Transitive and Symmetric Nonrigid Image Registration

A Thesis
Presented to
The Academic Faculty

by

Yi-Yu Chou

In Partial Fulfillment
of the Requirements for the Degree
Master of Science

School of Biomedical Engineering
Georgia Institute of Technology
April 2004

Transitive and Symmetric Nonrigid Image Registration

Approved by:

Dr. Oskar Skrinjar, Adviser

Dr. Paul Benkeser

Dr. James M. Rehg

Date Approved: April 6. 2004

ACKNOWLEDGEMENTS

I would like to express my appreciation to Dr. Skrinjar for his advice during my graduate research at Georgia Tech. As my advisor, he has constantly forced me to remain focused on achieving my goal. His observations and comments helped me to establish the overall direction of the research and to move forward with investigation in depth.

I would also like to thank my parents who gave me the opportunity to study. Without their support, I would have never got this far. Finally, I would like to dedicate this thesis to my wife, Yi-Chun, for her love, patience, and understanding.

Yi-Yu Chou

Atlanta, April 2004

TABLE OF CONTENTS

ACKNOWLEDGEMENTS . . . . . **iii**

LIST OF TABLES . . . . . **vii**

LIST OF FIGURES . . . . . **viii**

SUMMARY . . . . . **x**

Chapter 1 INTRODUCTION **1**

1.1 What is Image Registration? 1

1.2 Why do We Need Image Registration? 1

1.3 Classification of Image Registration 2

1.4 Contributions of This Thesis 3

Chapter 2 AN OVERVIEW OF REGISTRATION TECHNIQUES . . . **5**

2.1 Feature Space 5

2.1.1 Feature-based registration 5

2.1.2 Intensity-based registration 6

2.1.3 Hybrid registration 6

2.2 Warp Space 6

2.2.1 Basis function expansions 7

2.2.2 Physical models 7

2.2.3 Optical flow methods 8

Chapter 3 A REGISTRATION ALGORITHM **9**

3.1 Transformation and Resampling 10

3.2 Image Warping Methods 10

3.2.1 Thin-plate spline 11

3.2.2 Cubic B-spline 12

3.3 Image Similarity Measure 13

3.3.1 Mean square differences 14

3.3.2 Correlation coefficient 14

3.3.3 Mutual information 15

3.4 Optimization 16

3.4.1 Gradient-descent method 16
3.4.2 Hierarchical multi-scale strategy 16
Chapter 4 REGISTRATION PROPERTIES 18
4.1 Transitivity property 18
4.2 Symmetry Property 21
4.2.1 Symmetry for a sequence of images 22
4.2.2 Symmetry for image pairs 23
Chapter 5 VALIDATION STRATEGIES 24
5.1 Validation Strategies Suggested in the Literature 24
5.1.1 Visual Assessment 25
5.1.2 Gold Standard 25
5.1.3 Simulation 25
5.1.4 Consistency 26
5.1.5 Specialized Methods 26
5.2 2D Validation Data 27
5.3 3D Validation Data 28
5.4 Manual Validation 31
Chapter 6 EXPERIMENTAL RESULTS 32
6.1 Nonrigid image registration 32
6.1.1 2D nonrigid registration 32
6.1.2 3D nonrigid registration 33
6.2 Transitivity 39
6.2.1 2D transitivity 39
6.2.2 3D transitivity 40
6.3 Symmetry 40
6.3.1 2D symmetry 46
6.3.2 3D symmetry 46
6.4 New Validation Strategies 52
6.4.1 2D validation strategy 52
6.4.2 3D validation strategy 56

Chapter 7 DISCUSSION AND CONCLUSION 57

REFERENCES 59

LIST OF TABLES

Table 1 The maximum error for 2D nonrigid image registration by thin-plate spline with mean squared differences. 33

Table 2 The maximum error for 2D nonrigid image registration by cubic B-spline with normalized mutual information. 34

Table 3 The maximum error for 3D nonrigid image registration. 39

Table 4 The transitivity error (max, mean std) for random triples of images (I_1, I_2, I_3) with a given model (M) from the first sequence of 2D short axis cardiac MR images. 40

Table 5 The transitivity error (max, mean std) for random triples of images (I_1, I_2, I_3) with a given model (M) from the second sequence of 2D short axis cardiac MR images. 41

Table 6 The transitivity error (max, mean std) for random triples of images (I_1, I_2, I_3) with a given model (M) from the 3D short axis cardiac MR images. . . . 41

Table 7 The symmetry error(max, mean std) for random pair of images (I_1, I_2) with a given model (M) from the first sequence of 2D short axis cardiac MR images. 47

Table 8 The symmetry error(max, mean std) for random pair of images (I_1, I_2) with a given model (M) from the second sequence of 2D short axis cardiac MR images. 47

Table 9 The symmetry error(max, mean std) for random pair of images (I_1, I_2) with a given model (M) from the second sequence of 2D short axis cardiac MR images. 52

Table 10 The average error for five observers for twenty markers for case 2. 54

Table 11 The mean and maximum value of the average error for five observers over the twenty markers. 55

Table 12 The mean and maximum error value of markers with salient anatomical features. 55

Table 13 The correlation coefficient of standard deviation and error for markers with salient anatomical features from case 1 to case 6. 56

Table 14 The mean and maximum value of the average error for four observers over the twenty markers in 3D experiment 56

LIST OF FIGURES

Figure 1 The classification of image registration. 3

Figure 2 The flowchart of the nonrigid image registration algorithm. 9

Figure 3 A transformation T applied to the pixel center in I_2^*, and the corresponding point in the coordinate system to the object image I_2. 11

Figure 4 Multi-scale strategy. 17

Figure 5 Notation used to describe transformations from one coordinate system to another. 19

Figure 6 The new registration operator. 20

Figure 7 The forward transformation $\Gamma(I_1, I_2)$ from image I_1 to I_2 and the reverse transformation $\Gamma(I_2, I_1)$ from image I_2 to I_1. 22

Figure 8 Optical warper. 27

Figure 9 Grid images and medical images for two cases acquired by the CCD camera. 29

Figure 10 A section through the 3D MRI volume of the deformable model. 30

Figure 11 Bead removal example 31

Figure 12 Nonrigid registration for 2D T1 weighted coronal brain images. 34

Figure 13 Nonrigid registration for 2D short axis MR cardiac images. 35

Figure 14 Three orthogonal slices of a 3D cardiac short axis MR image. 36

Figure 15 3D nonrigid registration test for case 1. 37

Figure 16 3D nonrigid registration test for case 2. 38

Figure 17 2D transitivity test for case 1. 42

Figure 18 2D transitivity test for case 2. 43

Figure 19 3D transitivity test for case 1. 44

Figure 20 3D transitivity test for case 2. 45

Figure 21 2D symmetry test for case 1. 48

Figure 22 2D symmetry test for case 2. 49

Figure 23 3D symmetry test for case 1. 50

Figure 24 3D symmetry test for case 2. 51

Figure 25 A pair of images and a set of corresponding points displayed over the images were generated by the automated method. 53

Figure 26 (a) A sample scatter plot of the standard deviation versus error of markers with salient anatomical features. (b) The scatter plot of the average value of the mean standard deviation versus the errors for all six cases. 55

SUMMARY

The main topic of this thesis is nonrigid image registration for medical applications. We start with an overview and classification of existing registration techniques. We develop a general nonrigid image registration algorithm. It uses spline functions to describe the deformation and uses multi-scale strategy to search for the optimal transformation. Then we present a new registration operator that is transitive and symmetric. We investigate the theoretical implication of these properties and apply this operator to the registration of sequences of MR cardiac images.

In the second part of the thesis, two methods, one 2D and one 3D, for validation of nonrigid image registration algorithms are proposed and compared to a manual validation strategy. Both methods provide pairs of deformed images as well as corresponding true displacement fields with known accuracy. Nonrigid registration algorithms can be run on the pairs of images and their outputs can be compared to the true displacement fields that were generated manually by five observers. While these phantom validation studies do not provide physically correct deformations, they are certainly a useful way to test the algorithm's ability to recover various deformation patterns.

CHAPTER 1

INTRODUCTION

1.1 What is Image Registration?

Image registration is the process of aligning images so that corresponding features can easily be related [1].

We will call a registration "nonrigid", if the distances between image points are not preserved under the transformation, i.e. the transformation is not globally isometric.

1.2 Why do We Need Image Registration?

Image registration can serve as a powerful tool to investigate how regional anatomy is altered in disease, with age, gender, handedness, and other clinical or genetic factors. One of the most obvious clinical applications of registration is the area of serial imaging. Comparison of scans from a given patient acquired over various time intervals can be routinely performed to follow disease progression, response to treatment and even dynamic patterns of structure change during organ development. Unfortunately, diagnostic imaging scans are not routinely registered in most radiology department; in contrast, the common practice for an examiner is to do one's best to look at film montages of slices that do not match and try to access disease changes. For gross changes this method of comparison may be adequate. For subtle changes, visual comparison of unmatched images is not enough.

Image registration can also fuse information from multiple imaging devices to correlate different measures of brain structures and function. Integration of functional and anatomical imaging provides complementary information not available from independent analysis of each modality. Registered high-resolution anatomy in magnetic resonance imaging (MRI), ultrasound (US), or computed tomography (CT) images provides a much more precise anatomical basis for the interpretation of functional and pathologic image data, like single emission computed tomography (SPECT), positron emission tomography (PET), and

functional MRI (fMRI). Without registration, the observed activity would be less accurately mapped to the corresponding anatomical structures. Most importantly, intermodality registration can aid interpretation of clinical imaging for critically important treatment decisions.

Registration algorithms can encode patterns of anatomic variability in large human populations and can use the information to create a disease-specific, population-based brain atlas. This is a standard brain which is constructed from a number of brains and given in a fixed coordinate system to contain information about physical properties of neuroanatomies. When we have mapped an object and an atlas to each other, we can remove individual anatomical variation and pass segmentation or labeling information from the atlas to the subject image.

Many surgical procedures require highly precise localization, often of deeply buried structures, in order for the surgeons to extract targeted tissue with minimal damage to nearby structures. The plan is constructed in the coordinate system relative to preoperative image data, while the surgical procedure is performed in the coordinate system relative to the patient. Although methods such as MRI and CT are invaluable in imaging and displaying the internal structure of the body, the surgeons still face a key problem in applying that information to the actual procedure. With the help of registration, the relationship between preoperative data and patient coordinate system can be established, and thus provides the surgeon information about position of his instruments relative to the planned trajectory, and allows the surgeon to directly visualize important structures, and act accordingly.

1.3 Classification of Image Registration

Image registration can be classified into rigid, affine, projective and nonrigid, based on the geometric transformation. A 3D rigid transformation preserves the distances and angles between points, and can be represented by three translation vectors and three rotation angles (6 degree of freedom). An affine transformation amounts to a rigid transformation plus three Cartesian scale factors and shears (12 degree of freedom), which maps parallel lines to parallel lines but does not conserve the angles between lines. A projective transformation preserves the straightness of lines but not the parallelism. A nonrigid transformation does

not preserve the straightness of lines and, in general, maps a line into a curve. For the remainder of this research, we will consider nonrigid transformations that guarantee that connected subregions remain connected, neighborhood relationships between structures are preserved, and surfaces are mapped to surfaces. A nonrigid transformation can not generally be expressed in a matrix notation and it involves a lot of parameters. Therefore, it has a much larger number of degrees of freedom than a rigid or affine transformation and has more flexibility to accommodate local shape differences (see Fig.1).

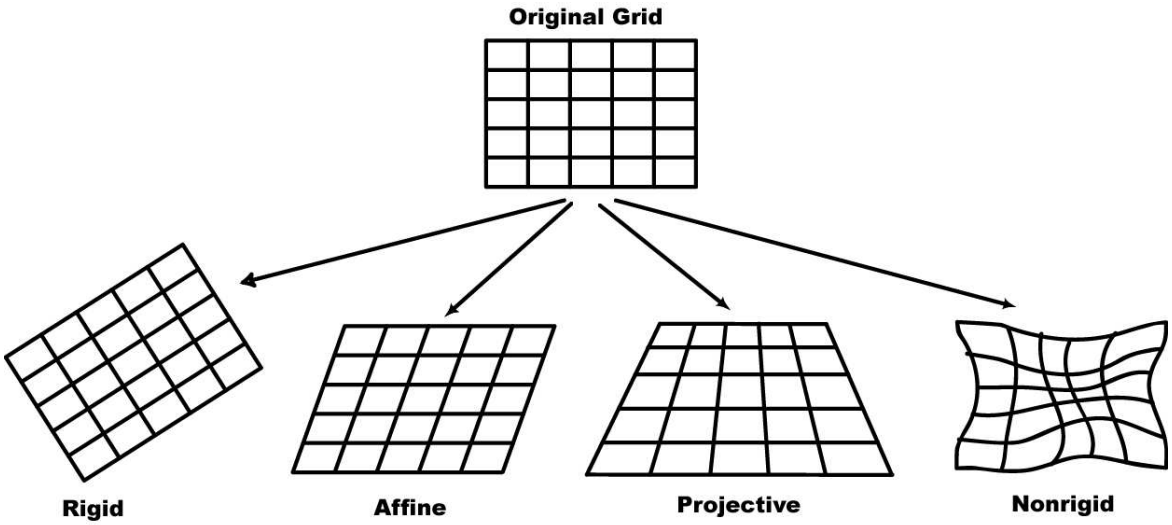

Figure 1: The classification of image registration: rigid, affine, projective and nonrigid.

1.4 Contributions of This Thesis

The first contribution of this thesis is the implementation of a general nonrigid image registration algorithm. It uses a set of warping function (thin-plate spline or cubic B-spline) to model the deformation, and it uses the intensity-based matching to compute the image similarity by the method of mean square differences or normalized mutual information. A generalized version of this algorithm that is significantly faster and capable of treating two dimensional and three dimensional deformations is presented in Chapter 3.

The second contribution of this thesis is the development of transitivity and symmetry for the nonrigid image registration algorithms. In Chapter 4, we give a definition for these properties, and in Chapter 6, we quantitatively show that the transitive and symmetric

property is achieved in both 2D and 3D nonrigid image registration algorithms.

The third contribution of this thesis is the development of two new methods, one 2D and one 3D, for generation of validation data for nonrigid image registration algorithms. In Chapter 5, we describe the strategies for validation and in Chapter 6, we discuss the experimental results.

CHAPTER 2

AN OVERVIEW OF REGISTRATION TECHNIQUES

In this chapter we intend to categorize the multitude of existing nonrigid registration techniques. We classify them by the choice of feature space and warp space.

2.1 Feature Space

Many techniques that have been proposed to solve the registration problem in many different forms can be broadly classified into three types, namely feature-based matching, intensity-based matching and hybrid approaches. Each of these approaches has its advantages and disadvantages.

2.1.1 Feature-based registration

Feature-based approaches attempt to find the correspondence and transformation using distinct anatomical features that are extracted from images. These features include points ([2]; [3]; [4]), curves ([5]; [6]; [7]), or a surface model ([8]; [9]; [10]) of anatomical structures. Feature-based methods are typically applied when the local structure information is more significant than the information carried by the image intensity. They can handle complex between-image distortions and can be faster, since they don't evaluate a matching criterion on every single voxel in the image, but rather rely on a relatively small number of features. The simplest set of anatomical features is a set of landmarks. However, the selection of landmarks is recognized to be a difficult problem, whether done automatically or manually. For many images, this is a serious drawback because registration accuracy can be no better than what is achieved by the initial selection of landmarks. For practical reasons, the number and precision of landmark locations is usually limited. Hence, spatial coordinates and geometric primitives often oversimplify the data by being too sparse and imprecise.

2.1.2 Intensity-based registration

The intensity-based registration methods operate directly on the image gray values, without reducing the gray-level image to relatively sparse extracted information. The basic principle of intensity-based techniques is to search, in a certain space of transformations, the one that maximizes (or minimizes) a criterion measuring the intensity similarity of corresponding voxels. Some measures of similarity are sum of squared differences in pixel intensities ([11]; [12]), regional correction ([13]), or mutual information ([14]). Mutual information has proved to be an excellent similarity measure for cross-modality registrations, since it assumes only that the statistical dependence of the voxel intensities is maximal when the images are geometrically aligned. The intensity similarity measure, combined with a measure of the structural integrity of the deforming scan, is optimized by adjusting parameters of the deformation field. Such an approach is typically more computationally demanding, but avoids the difficulties of a feature extraction stage. Further discussion of image similarity measures are given in section 3.3.

2.1.3 Hybrid registration

Further hybrid approaches, based on a combination of feature-based and intensity-based criteria, are likely to benefit from both the advantages of each strategies. Christensen et al. [15] introduced a hierarchical approach to image registration combining a landmark-based scheme with a intensity-based approach using a fluid model. The approach has been applied to the registration of 3D cryosection data of a macaque monkey brain as well to MR images of the human brain.

2.2 Warp Space

One of the important factors to categorize registration techniques is the warp space used, because it contains warping functions. Warping functions are candidate solutions of the registration problem. These exhibit the wide range of methods developed over the last twenty years and include the basis-function expansions, physical models, and optical flow methods.

2.2.1 Basis function expansions

Nonrigid registration produces a deformation field, giving a mapping for each pixel (voxel) in the deforming image. The deformation may be expressed in terms of a truncated set of basis functions. Specific examples include sinusoidal or wavelet basis ([16]; [17]) and radial basis functions such as thin-plate splines ([18];[19]). Compactly supported basis function such as B-splines ([20]; [21]; [22]) or other radially symmetric compactly supported basis functions have also been used. The algorithms of thin-plate spline and cubic B-spline will be further discussed in section 3.2.

2.2.2 Physical models

Nonrigid image registration can also be performed by modeling the deformation of the source image into the target image as an elastic physical process. A wide range of these methods ([23]; [24])are based on Navier-Stokes linear elastic partial differential equation:

$$\mu\Delta \mathrm{u}(\mathrm{x})+(\mu+\lambda)\nabla(\nabla\cdot \mathrm{u}(\mathrm{x}))=\mathrm{k}(\mathrm{x},\mathrm{u}(\mathrm{x})),$$

where μ and λ is the Lam*é* constant, which refer to the elastic properties of the medium. $\mathrm{u} = (\mathrm{u}_1,\mathrm{u}_2,\mathrm{u}_3)$ is the displacement field, and k is the force acting on the elastic body. The term $\Delta = \nabla^T\nabla$ is the Laplacian operator and $\nabla(\nabla\cdot\mathrm{u})$ is gradient of the divergence of u. Generally λ is set to zero to ensure that deformations are only effect in the directions of applied forces; μ takes a value between 0 and 1. The external forces can be derived from the local optimization of the similarity function which is defined by the intensity values or by the correspondence of boundary structures.

Navier-Stokes equation has a disadvantage of disallowing extensive localized deformations due to the modeling of stresses that increase proportionally to deformation strength. This can be handled by viscous fluid model ([25]; [26]). Instead of using the displacement directly in Navier-Stokes equation, the deformation velocity v is used.

$$\mu\Delta \mathrm{v}(\mathrm{x})+(\mu+\lambda)\nabla(\nabla\cdot \mathrm{v}(\mathrm{x}))=\mathrm{k}(\mathrm{x},\mathrm{u}(\mathrm{x})).$$

The advantage of using the velocity is that we can allow large deformations which can not be performed by the Navier-Stokes equation alone. A resulting problem is that the

likelihood of misregistrations is increased.

2.2.3 Optical flow methods

The optical flow constraint equation was derived to estimate the motion between two successive frames in an image sequence. It is based on the assumption that the intensity value of a given point in the image does not change over small time increments. The constraint can be expressed as :

$$(\nabla I)^T \cdot \vec{v} + I_t = 0$$

in which ∇I, $\vec{v}$, and I_t are the intensity gradient of the image, the unknown motion vector between the images, and the temporal derivative of the image, respectively. This equation is underconstrained (a problem known as the aperture problem) and a number of regularization scheme have been proposed to address this problem ([27]; [28]).

CHAPTER 3

A REGISTRATION ALGORITHM

A registration method that determines the correspondences between images by optimizing an image intensity similarity measure is considered in this research. Fig. 2 is the representation of flow of my registration algorithm. Image I_1 is the target image and I_2 is the deformed image. This algorithm consists of three main stages: 1) a warping function `T` that spatially transforms I_2 into $I_2{}^*$. 2) a function that measures the similarity between I_1 and $I_2{}^*$. 3) an optimization stage that searches for the optimal transformation.

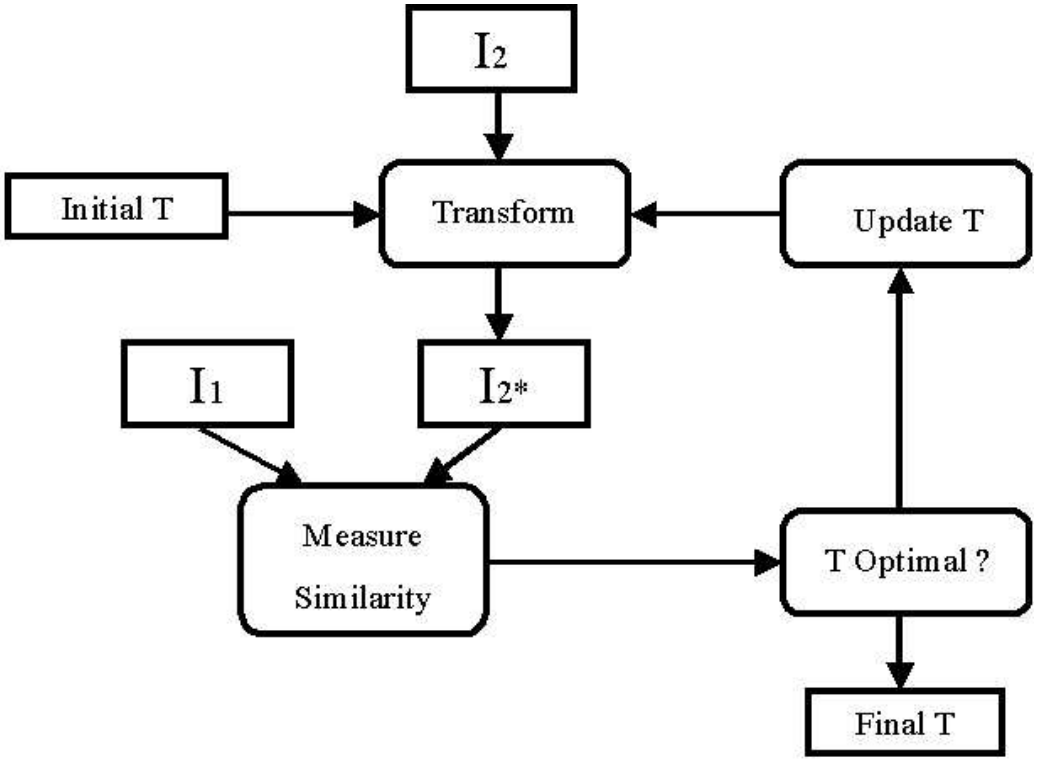

Figure 2: The flowchart of the nonrigid image registration algorithm.

3.1 Transformation and Resampling

We call the target image the template (I_1), and the image we want to deform the object image (I_2). The transformation we seek is actually a transformation of coordinates of each sampled point to new coordinates which will give us a new intensity value and generates a deformed image ($I_2{}^*$). The images we will register I_1 and I_2, do not necessarily have the same number of pixels and pixel size [mm]. Suppose we found a transformation, T, that will perform the map we want to apply, then this transformation will transform each pixel (voxel) center of the target image to an new point in the coordinate system of the object image. This new point is then not necessarily falls on the pixel (voxel) center in this new coordinate system. Because of this, we have to find the intensity value for the image (I_2) in each pixel (voxel) center in the coordinate system of the target image. This can be done by using the inverse transformation on each pixel (voxel) center, and find the corresponding point in image (I_2).

However, it would be difficult to get the inverse function directly especially for the non-rigid image transformation functions. Here we used another way to compute the deformed image ($I_2{}^*$). First, we set ($I_2{}^*$) to be the same dimensions and pixel (voxel) size as the target image (I_1). Then, through the transformation function T, we map each pixel (voxel) center in ($I_2{}^*$) to a new point in the object image (I_2), and compute its intensity value by interpolating with the neighboring pixel (voxel) centers (see Fig.3). This relationship between ($I_2{}^*$) and (I_2) can be expressed as:

$$I_2{}^* = I_2(\mathtt{T}),$$

3.2 Image Warping Methods

In this research, a deformation is defined on a sparse, regularly distributed grid of control points placed over the object image and is then varied by defining the motion of each control point. We implemented two algorithms, thin-plate spline and cubic B-spline, for the nonrigid image warping. Both the methods have been shown to possess at least C^2 continuity, which is important in medical image registration problem, since we need continuous and smooth

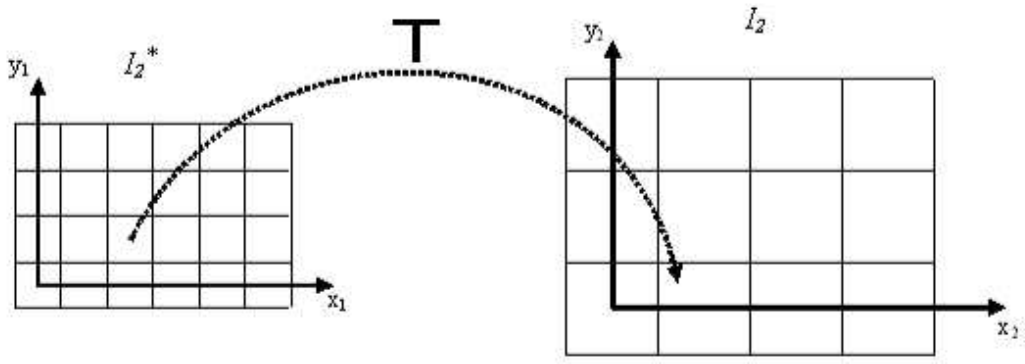

Figure 3: A transformation T applied to the pixel center in I_2^*, and the corresponding point in the coordinate system to the object image I_2.

functions to describe the deformation patterns.

3.2.1 Thin-plate spline

Thin-plate splines have a physical motivation. They interpolate specified points while minimizing a 2D bending energy,

$$\int (\frac{\partial^2 z}{\partial x^2})^2 + 2(\frac{\partial^2 z}{\partial x \partial y})^2 + (\frac{\partial^2 z}{\partial y^2})^2 \tag{1}$$

resulting in a smooth deformation without unexpected ripples and variations. The fundamental basis function used by the 2D thin-plate spline is given by the following expression,

$$z(x,y) = -U(r) = -r^2 \log r^2 \tag{2}$$

where r is the distance $\sqrt{(x^2 + y^2)}$ from the Cartesian origin. The function $U(r)$ satisfies the following equation.

$$\delta^2 U = (\frac{\partial^2}{\partial x^2} + \frac{\partial^2}{\partial y^2})^2 U \propto \delta_{0,0} \tag{3}$$

Thus, U is a fundamental solution of the biharmonic equation $\Delta^2 = 0$, the equation for the shape of a thin metal plate vertically displaced as a function z(x,y) above the (x,y) plane. For the 3-dimensional situation, the fundamental solution of the biharmonic equation is $U(r) = |r|$.

A component (x or y) of the thin-plate spline displacement field can be expressed as [2]

$$f(x,y) = a_1 + a_x x + a_y y + \sum_{i=1}^{n} w_i U(|P_i - (x,y)|) \tag{4}$$

where a_1, a_x, and a_y define the affine transformation. The unknown parameters W = $[w_1, w_2, ...w_n]$ in Eq.(4) are determined by solving the linear system of equations that result by fixing the displacement field values at landmark locations. Let $P_1 = (\mathrm{x}_1, y_1)$, $P_2 = (\mathrm{x}_2, y_2)$,...,$P_n = (\mathrm{x}_n, y_n)$ be n points in the ordinary Euclidean plane, $r_{ij} = |P_i$ - $P_j|$ for the distance between points i and j, and build the matrix

$$L = \begin{bmatrix} K & P \\ P^T & \mathrm{O} \end{bmatrix}, and$$

$$K = \begin{bmatrix} 0 & U(r_{12}) & ... & U(r_{1n}) \\ U(r_{21}) & 0 & ... & U(r_{2n}) \\ ... & ... & ... & ... \\ U(r_{n1}) & U(r_{n2}) & ... & 0 \end{bmatrix}$$

$$P = \begin{bmatrix} 1 & x_1 & y_1 \\ 1 & x_2 & y_2 \\ ... & ... & ... \\ 1 & x_n & y_n \end{bmatrix}$$

where O is a 3 x 3 matrix of zeros. Also, define a landmark displacements as D = $[d_1, ...d_n, 0, 0, 0]^T$. The equation formed by substituting the landmark constrains into Eq.(4) can be written in matrix form as $D = L\,W$. The solution W to this matrix equation is determined by least squares estimation since the matrix K is not guaranteed to be full rank.

3.2.2 Cubic B-spline

For the 3D cubic B-spline warping methods, the transformation T is defined by a grid Φ, a $n_x \times n_y \times n_z$ lattice of uniformly spaced control points $\phi_{i,j,k}$. The spacing between the control points in x, y and z directions are denoted by δ_x, δ_y, and δ_z, respectively. At any position $X = (x,y,z)$ the deformation is computed from the positions of the surrounding 4

x 4 x 4 neighborhood control points

$$T(X) = \Sigma_{l=0}^{3}\Sigma_{m=0}^{3}\Sigma_{n=0}^{3} B_l(u)B_m(v)B_n(w)\phi_{i+l,j+m,k+n} \tag{5}$$

Here, *i,j* and *k* denote the index of the control point cell, containing $X = (x,y,z)$, and *u,v,* and *w* are the relative positions of *x*, *y*, and *z*, respectively. Where $i = \lfloor \mathrm{x}/\delta_x \rfloor$ - 1, $j = \lfloor \mathrm{y}/\delta_y \rfloor$ - 1, $k = \lfloor \mathrm{z}/\delta_z \rfloor$ - 1, $u = \mathrm{x}/\delta_x$ - $\lfloor \mathrm{x}/\delta_x \rfloor$, $v = \mathrm{y}/\delta_y$ - $\lfloor \mathrm{y}/\delta_y \rfloor$, and $w = \mathrm{z}/\delta_z$ - $\lfloor \mathrm{z}/\delta_z \rfloor$. The functions B_0 through B_3 are the third-order basis functions of the B-spline.

$$\begin{aligned} B_0(t) &= (1-t)^3/6 \\ B_1(t) &= (3t^3 - 6t^2 + 4)/6 \\ B_2(t) &= (-3t^3 + 3t^2 + 3t + 4)/6 \\ B_3(t) &= t^3/6 \end{aligned}$$

In contrast to thin-plate spline, cubic B-splines that define the geometrical transformation model described above have two different mathematical properties: they are locally controlled (i.e., changing the position of a control point affects the transformation only in the 4 x 4 x 4 neighborhood of the control points), and they are approximating rather than interpolating functions. Related applications can be found in Ref.[29].

3.3 Image Similarity Measure

Nonrigid image registration is an optimization problem, where the goal is to optimize an image similarity measure with respective to the transformation parameters. This approach defines an image registration operator. E.g. one can write

$$\Gamma(I_1, I_2) = arg\ min_T E(I_1, I_2 \circ \mathrm{T}) \tag{6}$$

where E is a cost (energy) function, and T is a geometric transformation function. Sometimes, in addition to the similarity measure term, the cost function to be minimized contains as well so-called smoothness term, which help to smooth and prevent folding of the transformation. By adding a smoothness term to the equation, one obtains,

$$\Gamma(I_1,I_2) = arg\ min_T[E(I_1,I_2\circ \mathrm{T}) + E_{smooth}(\mathrm{T})].$$

A general form of such a smoothness term has been described by Wahba[30]. In 3D situations, the smoothness term often takes the following form:

$$E_{smooth} = \frac{1}{V}\int_0^X \int_0^Y \int_0^Z [(\frac{\partial^2 T}{\partial x^2})^2 + (\frac{\partial^2 T}{\partial y^2})^2 + (\frac{\partial^2 T}{\partial z^2})^2 + 2(\frac{\partial^2 T}{\partial xy})^2 + 2(\frac{\partial^2 T}{\partial xz})^2 + 2(\frac{\partial^2 T}{\partial yz})^2] dxdydz$$

where V denotes the volume of the image.

Examples of similarity measures are mean square differences, correlation coefficient, and mutual information. In feature-based registration or in matching of curves and surfaces, it is common to use a geometric distance as a measure of the similarity.

3.3.1 Mean square differences

One of the simplest image similarity measure is the mean square differences between images A and B, *MSD*, which is minimized during registration ([31], [32]). For N pixels (voxels) in the overlap domain $\Omega_{A,B}$, MSD is given by

$$MSD = \frac{1}{N}\sqrt{\sum_{x\epsilon\Omega_{A,B}} \mid A(x) - B(x) \mid^2} \tag{7}$$

It is necessary to divide by the number of pixels (voxels) N in the overlap domain because N may be vary with each estimate of transformation. It can be shown that this is the optimum measure when the two images only differ by Gaussian noise. It is quite obvious that for multimodality registration this will never be the case. The strict requirement is seldom true in unimodality registration either, as noise in the medical images is frequently not Gaussian, and also because it is likely that the object being imaged undergoes a change between acquisitions.

3.3.2 Correlation coefficient

The *MSD* measure makes the implicit assumption that after registration, the image differ only by Gaussian noise. A slightly less strict assumption would be that, at registration, there is an affine relationship between the intensity values in the images. In this case, the optimum similarity measure is the Correlation coefficient, *CC*.

$$CC = \frac{\sum_{x\epsilon\Omega_{A,B}^T}(A(x) - \bar{A})(T(B(x)) - \bar{B})}{[\sum_{x\epsilon\Omega_{A,B}^T}(A(x) - \bar{A})^2(T(B(x)) - \bar{B})^2]^{1/2}} \tag{8}$$

where $\bar{A}$ is the mean intensity value in image $\mathrm{A}|_{\Omega^T_{A,B}}$ and $\bar{B}$ is the mean of $\mathrm{B}|_{\Omega^T_{A,B}}$. This measure will give values in the interval [-1,1], and has to be maximized to register the images ([33]).

3.3.3 Mutual information

In recent years, many image similarity measures based on joint entropy, mutual information (MI), and normalized mutual information (NMI), have shown promising results for multimodality image registration. Registration of multimodal images is a difficult task, but often necessary to be solved, especially in medical imaging applications. The comparison of anatomical and functional images of the patient's body can lead to a diagnosis that would be impossible to gain otherwise. The MI, originating from the information theory, is a measure of statistical dependency between two data sets. MI between two random variables A and B is given by

$$\begin{aligned} MI(A,B) &= H(B) - H(B|A) = H(A) + H(B) - H(A,B) \\ H &= -\sum_i p_i \log p_i \\ H(A,B) &= -\sum_{a \epsilon A} \sum_{b \epsilon B} p_{AB}(a,b) \log p_{AB}(a,b) \end{aligned}$$

where H is the average information supplied by a set of n symbols (image intensities) whose probability are given by p_1, p_2, p_3,..., p_n. $H(A,B)$ is the joint entropy, and the values in each element represent the probability of pairs of image values occurring together.

In particular, p_{AB}(a,b) is very dependent on the joint overlap $\Omega^T_{A,B}$, which is undesirable. To reduce the effect of the dependence on volume of overlap we should normalize to the combined information in the overlapping volume. The following equation defines normalized mutual information

$$NMI(A,B) = \frac{H(A) + H(B)}{H(A,B)} \tag{9}$$

For more information about the mutual information based registration of medical images, see Ref. [34]

3.4 Optimization

Finding the minimum of dissimilarity measure or the maximum of similarity measure is a multidimensional optimization problem, where the number of dimensions corresponds to the degrees of freedom of the geometrical transformation. In case of transformations with more degrees of freedom or in case of more complex similarity measures, sophisticated optimization algorithms are required.

3.4.1 Gradient-descent method

When we minimize a cost function, we want to find the global minimum of this transformation function in a given domain. The most often used methods are gradient-descent methods. These methods numerically find a minimum by iteratively moving the current solution in the direction of the gradient by small steps. The gradient Δ was initially normalized to the length given by the current step size. If no further improvement was possible, the length of Δ was successively decreased by a factor of 2 until a user-defined minimum step size was reached. The optimization terminated when the global step size reached the user-defined minimum step size.

3.4.2 Hierarchical multi-scale strategy

One of the difficulties with optimization algorithms is that they may converge to an incorrect solution called a "local optimum". In theory, there will be more local optimum as the dimension of the transformation increases. A hierarchical multi-scale approach (coarse to fine strategy) to registration is common, in which the images are first registered at coarse spatial scale, then the transformation solution obtained at this scale is used as the starting estimate for registration at a finer one, and so on. The whole process is illustrated in Fig.4. This multi-scale approach ensures convergence of the optimization method and the transformation model is gradually made more complex so as to best describe the transformation between images. For many type of optimizers, this strategy for convergence is significantly faster than a single stage approach.

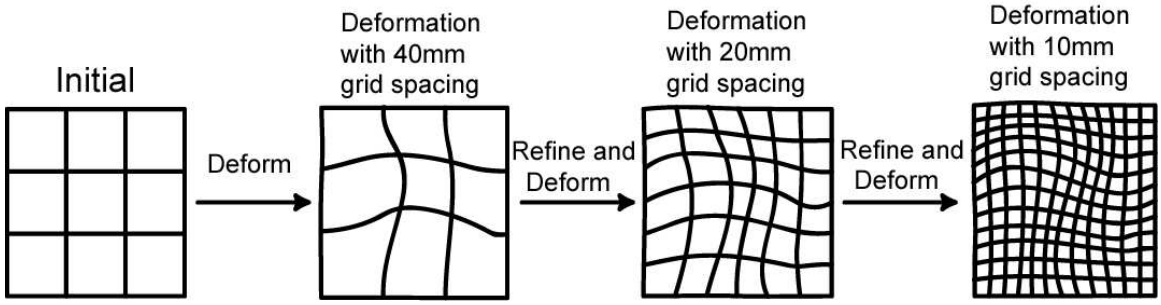

Figure 4: Multi-scale strategy: the complexity of the warp increases with the number of relatively displaced nodes.

CHAPTER 4

REGISTRATION PROPERTIES

Image registration can also be regarded as an algorithmic problem. It's very important to understand some basic properties of these algorithms. In this research, we discuss two properties: transitivity and symmetry of image registration algorithms.

4.1 Transitivity property

To avoid ambiguity a definition of the composition of two functions is given here.

Definition : The composition of functions $f_1 : B \mapsto C$ and f_2: $A \mapsto B$ is a function denoted as $f_1 \circ f_2$ that is defined by $f_1 \circ f_2$: $A \mapsto C$ and $(f_1 \circ f_2)(x) = f_1(f_2(x))$, $\forall x \, \epsilon A$

Problem Statement: For any three images, the generated transformation from the second to the third image composed with the generated transformation from the first to the second image should be equal to the generated transformation from the first to the third image (the order of transformations follows the Definition) (see Fig.5). This transitivity property can be formalized as

$$\Gamma(I_2, I_3) \circ \Gamma(I_1, I_2) = \Gamma(I_1, I_3) \tag{10}$$

The idea of transitivity of three transformations was first introduced in 2003 by Christensen ([38]). He investigated how an image registration algorithm that reduces the inverse consistency error can also reduce the transitivity error. The average transitivity error over a region of interest M was defined as

$$E(h_{AB}, h_{BC}, h_{CA}, \mathrm{M}) = \frac{1}{\mathrm{M}} \int_{\mathrm{M}} \| h_{AB}[h_{BC}[h_{CA}(x)]] - x \| \, dx \tag{11}$$

Where h_{AB}, h_{BC} and h_{CA} are transformations from image A to B, B to C and C to A, respectively. Although transitivity is a desirable property of nonrigid image registration algorithms, the algorithm Christensen used was not transitive.

The proposed approach [40] can be applied to any existing nonrigid (or rigid) image

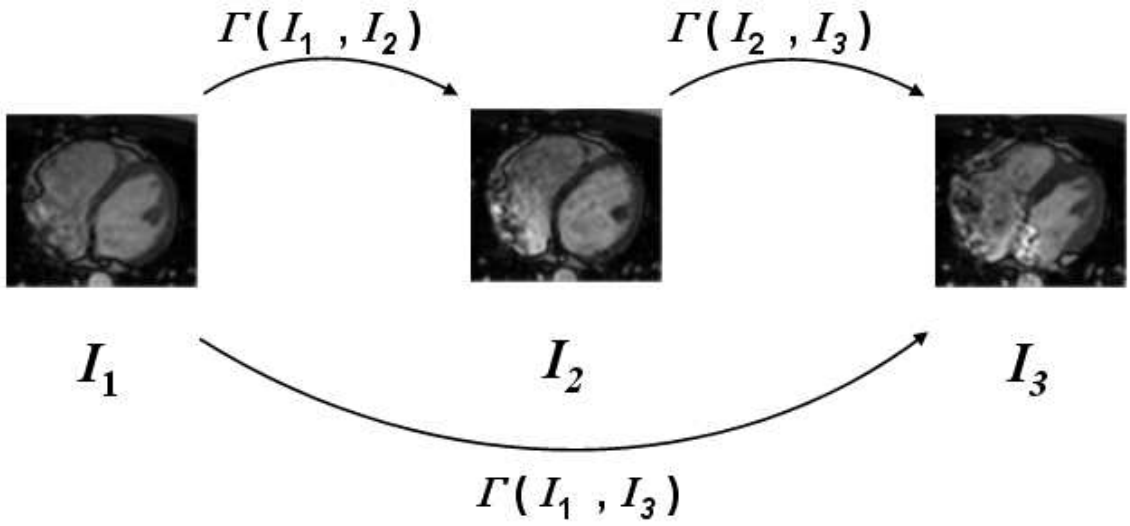

Figure 5: Notation used to describe transformations from one coordinate system to another.

registration algorithms, and mathematically guarantees that the transitivity property can be achieved. The first step is to select an image from the set (ex. a sequence of cardiac images), and refers it as the "model". Let the image registration operator be denoted as Γ and the model as M. A new image registration operator G is defined as

$$G(I_1, I_2) = [\Gamma(I_2, M)]^{-1} \circ \Gamma(I_1, M) \tag{12}$$

This new image registration operator G requires two operation of the original image registration operator Γ ($\Gamma(I_1, M)$ and $\Gamma(I_2, M)$), and also depends on the selected model image M. Thus, rather than registering two images directly, images are registered through a model (see Fig.6).

It's not difficult to see that G is transitive over the given set of images. For any three images (I_1, I_2, I_3) from the set,

$$\begin{aligned} G(I_1, I_2) &= [\Gamma(I_2, M)]^{-1} \circ \Gamma(I_1, M), \\ G(I_2, I_3) &= [\Gamma(I_3, M)]^{-1} \circ \Gamma(I_2, M), \\ G(I_1, I_3) &= [\Gamma(I_3, M)]^{-1} \circ \Gamma(I_1, M). \end{aligned}$$

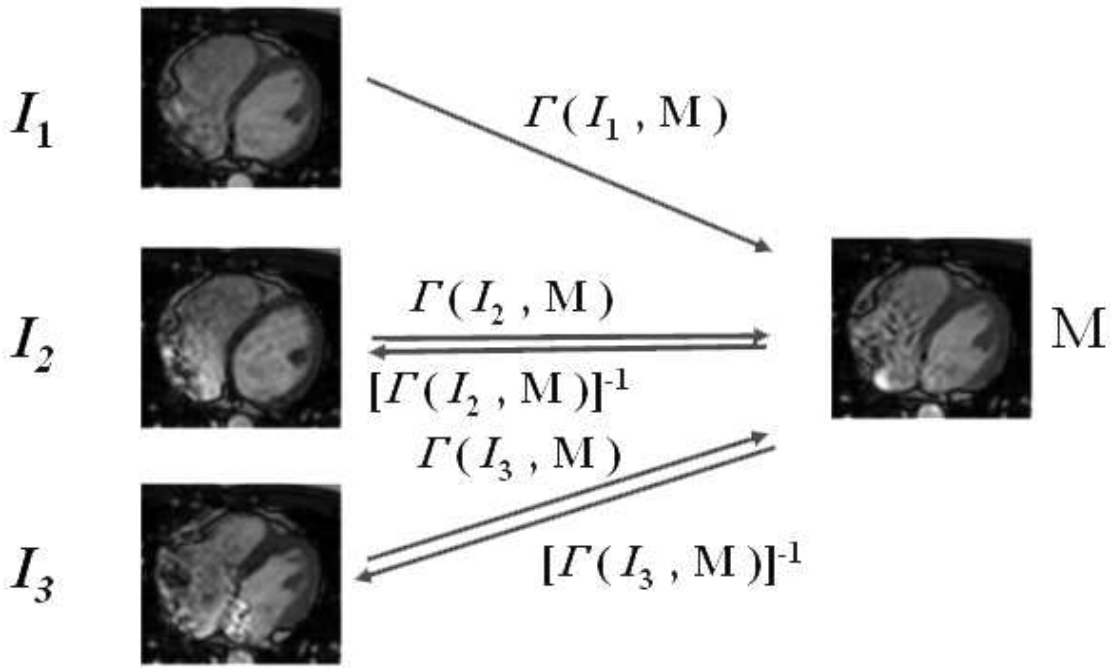

Figure 6: The new registration operator.

It follows that

$$\begin{aligned} G(I_2, I_3) \circ G(I_1, I_2) &= [\Gamma(I_3, M)]^{-1} \circ \Gamma(I_2, M) \circ [\Gamma(I_2, M)]^{-1} \circ \Gamma(I_1, M) \\ &= [\Gamma(I_3, M)]^{-1} \circ \Gamma(I_1, M) \\ &= G(I_1, I_3) \end{aligned}$$

proving that G is indeed transitive. Since transitivity has been proven mathematically, it means that it will always be satisfied regardless of the accuracy of the registration algorithms.

The procedure used to compute the inverse transformation is as follows. Assume that T is the forward transformation. It is possible to select a point y and iteratively search for a point x such that $||y - T(x)||$ is less than some threshold provided that the initial guess of x is close to the final value of x. The following procedure is used to compute the inverse T^{-1} of the transformation T.

For each sample point n do {

Set $\delta = [1,1,1]^T$, x = n.

While ($\delta >$ threshold) do {

δ = T(x) - n

x = x - $\delta/8$

}

$T^{-1}(n)$ = x

}

4.2 Symmetry Property

Problem Statement: When an image registration operator is applied to two (different) images, the obtained transformation should be the inverse of the transformation obtained when the order of images is reversed. This symmetry property can be formalized as

$$\Gamma(I_1, I_2) = [\Gamma(I_2, I_1)]^{-1} \tag{13}$$

where Γ denotes the image registration operator and I_1 and I_2 are any two images. The forward transformation $\Gamma(I_1, I_2)$ from image I_1 to I_2 and the reverse transformation and $\Gamma(I_2, I_1)$ from image I_2 to I_1 are shown in Fig. 7.

Many nonrigid image registration algorithms are not symmetric in part because the numerical optimization techniques used to find the optimal image transformation often get struck in local minima, and can't uniquely describe the correspondences between two images. Ideally, the constraint of this symmetry property will overcome the correspondence ambiguities and reduce the number of local minima because the problem is being solved from two different directions. The idea of symmetry was first introduced in 1998 by Woods et al., [12]. He averages the forward and the inverse linear transformations to reconcile differences between pairwise registration. In 1999 Christensen [35] proposed a consistent linear-elastic image registration algorithm ([36], [37], [38]) that jointly estimates the forward and reverse transformation between two images while minimizing the inverse consistency error between these transformations. Although this approach can minimize the difference between the

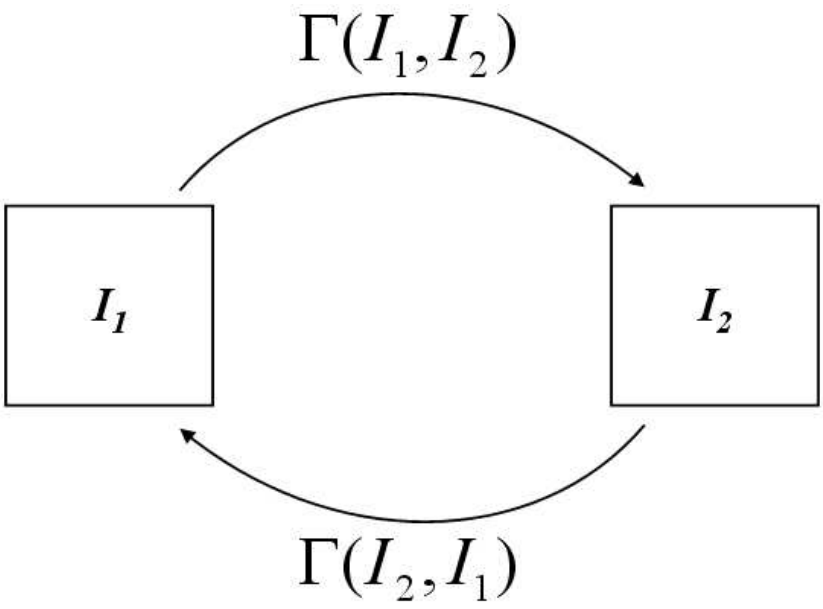

Figure 7: The forward transformation $\Gamma(I_1, I_2)$ from image I_1 to I_2 and the reverse transformation $\Gamma(I_2, I_1)$ from image I_2 to I_1.

forward and reverse transforation, it still can't guarantee the symmetric property to be satisfied exactly.

4.2.1 Symmetry for a sequence of images

If using the definition of Eq.12 to be the registration operator, the symmetric property will be satisfied and can be proven mathematically. Let the forward transformation be $\mathrm{G}(I_1, I_2) = \Gamma(I_2, M)^{-1} \circ \Gamma(I_1, M)$, and the reverse transformation be $\mathrm{G}(I_2, I_1) = \Gamma(I_1, M)^{-1} \circ \Gamma(I_2, M)$. The inverse function of the reverse transformation is:

$$\begin{aligned} \mathrm{G}(I_2, I_1)^{-1} &= \Gamma(I_2, M)^{-1} \circ [\Gamma(I_1, M)^{-1}]^{-1} \\ &= \Gamma(I_2, M)^{-1} \circ \Gamma(I_1, M) \\ &= \mathrm{G}(I_1, I_2) \end{aligned}$$

Therefore, the new registration operator G indeed satisfy the symmetric property. The disadvantage of this model-based approach is the require of the "model". Therefore, it's only suitable for registering a sequence of images and not for registering two images.

4.2.2 Symmetry for image pairs

To achieve the symmetric property for registering two images, Skrinjar and Tagare [39] presented an image registration operator, which is defined as:

$$\Gamma(I_1, I_2) = arg\, min_{T_{opt}}[E(I_1, I_2 \circ \mathrm{T}_{opt}) + E(I_2, I_1 \circ \mathrm{T}_{opt}^{-1})] \tag{14}$$

Let $\mathrm{T}_{12} = \Gamma(I_1,\ I_2) = \arg\ \min_{T_{opt}}[E(I_1, I_2 \circ \mathrm{T}_{opt}) + E(I_2, I_1 \circ \mathrm{T}_{opt}^{-1})]$. This means that the minimum of the energy function is $E(I_1, I_2 \circ \mathrm{T}_{12}) + E(I_2, I_1 \circ \mathrm{T}_{12}^{-1})$. Let $\mathrm{T}_{21} = \Gamma(I_2, I_1) = \arg\ \min_{\mathrm{T}_{opt}}[E(I_2, I_1 \circ \mathrm{T}_{opt}) + E(I_1, I_2 \circ \mathrm{T}_{opt}^{-1})]$, and the minimum of this energy function will be $E(I_2, I_1 \circ \mathrm{T}_{21}) + E(I_1, I_2 \circ \mathrm{T}_{21}^{-1})$. If $E(I_1, I_2 \circ \mathrm{T}_{12}) + E(I_2, I_1 \circ \mathrm{T}_{12}^{-1})$ equals to $E(I_2, I_1 \circ \mathrm{T}_{21}) + E(I_1, I_2 \circ \mathrm{T}_{21}^{-1})$, then $\mathrm{T}_{21} = \mathrm{T}_{12}^{-1}$. Thus, $\Gamma(I_1, I_2) = [\Gamma(I_2, I_1)]^{-1}$. They presented the experimental results by using piecewise-affine warping function to show that it satisfies the symmetric property with a very small numerical error.

The inverse of a piece-wise affine transformation can be computed exactly, because we can easily derive the analytical inverse function from the affine transformation matrix. For the thin-plate spline function, which requires two sets of control points to represent the deformations. One set of control points is fixed, and the other set represents the corresponding deformed points. If we reverse the order of these two sets of control points, we can get exactly inverse mapping over these control points. But the points in between are not inversive, because they are interpolated. Thus, T_{21} not equals to T_{12}^{-1}. For this reason, we discuss the symmetric properties based on the model-based approach in this thesis.

CHAPTER 5

VALIDATION STRATEGIES

One of the challenges in the development of image registration algorithms is their validation. The goal of rigid image registration in the case of alignment of 3D images is to compute the six parameters of the rigid body transformation[1]. The spatial transformation in the case of 3D non-rigid image registration is typically represented with thousands of parameters which renders the validation a much more challenging task compared to the validation of rigid image registration. In most practical situations it is either not possible or it is very difficult to obtain ground truth data for validation of non-rigid image registration.

Here we address the problem of validation of image registration algorithms. The ideal validation data for image registration of two images would have the true displacement vector for each point of the first image that would bring it to the corresponding point in the second image. In addition, the accuracy of the data has to be known, since validation data without known accuracy is useless. In most practical cases such data is impossible to obtain. Researchers have used a number of methods to assess the quality of image registration algorithms. In the next section we discuss the validation strategies suggested in the literature for the case of image registration of medical images. After that we present two methods, one 2D and one 3D, for generation of validation data for nonrigid image registration algorithms, followed by a comparison of the suggested methods to a manual validation strategy.

5.1 Validation Strategies Suggested in the Literature

Here we classify the validation strategies suggested in the literature for the image registration into five groups. For each group we discuss the advantages and disadvantages and

[1] E.g. these parameters can be the three components of the translation vector and three angles of rotation around the axes of the Cartesian coordinate system. Other choices of the six parameters are possible.

provide relevant references.

5.1.1 Visual Assessment

In many situation, the only practical approach for estimation of the registration accuracy is to visually inspect the images. Observers look at the registered images, using contour overlays for inter-modality registration [41], or difference images for intra-modality registration ([28], [29], [42], [36], [43], [44], [45], [46], [47]), then qualitatively classify the registration solution (e.g. as "good", "average", or "poor"). This is a subjective and qualitative measure and it does not provide true displacement vectors between the two images.

5.1.2 Gold Standard

If the true ("gold standard") geometric transformation between the two images is known, then the accuracy of the image registration algorithm can be obtained by comparing the calculated transformation to the "gold standard" one. For rigid image registration, this can be achieved by using bone-implanted markers [48] or stereotactic frames to provide the gold standard [49]. The invasive markers can be attached to cadavers or to surgical patients. After the image acquisition the markers can be removed from the images, followed by a linearly interpolated reconstruction in each missing region. These images can be used as test data for algorithms together with the known underlying rigid transformation which has a relatively high (sub-millimeter) accuracy [48]. While some image information is lost in the reconstruction, the main obstacle is the invasiveness of the procedure. This approach is suitable for the validation of rigid registration, since the geometric transformation is defined by only six parameters in the 3D case, and a relatively small number of markers is needed for a reliable estimation of the transformation parameters (e.g. in [48] 12 markers were used for registration). Such a method has not been used for the validation of nonrigid image registration since it would need a huge number of invasive markers.

5.1.3 Simulation

In the case of simulations, the accuracy of the generated data can be arbitrary high. One can generate a displacement field (i.e. geometric transformation) that will be referred to

as "true" displacement field, apply it to an image and obtain a deformed image. The image registration algorithm can be run using the original and the deformed image, and the computed displacements can be compared to the "true" ones ([50]). There are two main concerns about using simulations in assessment of image registration accuracy. First, the "true" displacement field is artificially generated, and it might not be a good representation of real displacement fields. The second problem is that the gray levels of corresponding points in the original and the artificially deformed image are either identical, or artificially altered, while in the case of real images the relationship between gray levels of the corresponding points can be very complex. To reduce the first problem, researchers in [51] used biomechanical modelling to generate more realistic displacement fields for validation of nonrigid image registration algorithms for the case of breast images.

5.1.4 Consistency

Let $\mathcal{T}(A, B)$ denote the geometric transformation between images A and B computed by the image registration algorithm under consideration. If the algorithm is perfect, then it should be inverse consistent, i.e. $\mathcal{T}(A, B) = \mathcal{T}^{-1}(B, A)$ should hold for any images A and B, where $\mathcal{T}^{-1}(B, A)$ is the inverse transformation of $\mathcal{T}(B, A)$. Similarly, a perfect image registration algorithm should be transitive, i.e. $\mathcal{T}(B, C) \circ \mathcal{T}(A, B) = \mathcal{T}(A, C)$ should hold for any three images A, B, C, where $\circ$ denotes the composition of transformations. While Christensen and Johnson built in the inverse consistency property into their nonrigid image registration algorithm [36], some researchers ([52], [53]) used inverse consistency and transitivity to test the validity of their image registration algorithms. This validity assessment approach, although quantitative, does not provide the ideal validation data: true displacements between the two images. However, if using Eq.(12) and (14) as your registration operator, this validation strategy is no longer valid. Since transitivity and symmetry are mathematically guaranteed of consistency.

5.1.5 Specialized Methods

These validation techniques are application specific, i.e. they can be used only with certain type of images. E.g. estimates of displacements representing tissue motion can be obtained

Figure 8: Optical warper placed in front of the CCD camera generates geometrically deformed images.

by using MR tagging ([54]) and MR phase velocity ([55]) imaging. These techniques are used in the deformation analysis of moving objects, like the heart. However, they cannot be used for validation of registration of e.g. pre- and post-operative brain images.

5.2 2D Validation Data

The proposed method uses a CCD camera and an optical system that geometrically deforms the acquired image. A 2D image is selected (in this experiment we used 2D slices from 3D medical image volumes), printed using a high-resolution printer, and then imaged by the CCD camera twice. First it is acquired directly, and the second time it is acquired in a deformed state by placing an optical system (see Fig.8) in between the camera and the printed image. The same process is repeated for a grid of lines printed on a piece of paper, which is positioned exactly where the printed image was placed when acquired by the camera. The grid is imaged first directly and then in a deformed state, where the geometric deformation is exactly the same as the one applied to the selected image. The intersections of the grid lines in both grid images (original and deformed) can be detected automatically. This provides a set of corresponding points between the image and its deformed version. A number of such validation sets can be generated by modifying the optical system. The accuracy of the method can be obtained from the thickness of the grid lines.

We have developed an algorithm for automated detection of the grid line intersections. We applied this algorithm to both undeformed and deformed grid images. For the six cases discussed here, the two grid images had 49 markers each. For all the cases the thickness of the grid lines was about 2 pixels. This means that the accuracy with which the grid line intersections can be determined is ± 1 pixel in each direction.

The grid images and the medical images were placed exactly the same relative to the CCD camera at the acquisition, and an identical deformation pattern was used to generate the deformed grid image and the deformed medical image. For this reason, the pairs of corresponding points obtained by computing the grid line intersections in undeformed and deformed grid images represent also corresponding points in the undeformed and deformed medical images. These point pairs can be used as validation points (with a known accuracy of 1 pixel) for testing nonrigid image registration algorithms.

Fig. 9 (a),(b),(e) and (f) show the undeformed grid and medical image for two cases, acquired from the printed grid and medical image pictures respectively by the CCD camera. By placing an optical warper(see Fig. 8 (a)) in front of the CCD camera, we can generate nonrigidly deformed grid and medical images as shown in Fig. 9 (c),(d),(g) and (h).

5.3 3D Validation Data

To generate ground truth data for validation of 3D nonrigid image registration algorithms we used a deformable physical model. We imaged the model in an MRI scanner, physically deformed the model, imaged it in the deformed state, and two more times deformed and then imaged the model. The model was made of two types of modelling clay and small pieces of carrot. The three components have different MR signals which made the contrast in the images and simulated anatomical structures. In addition, 20 small glass beads were placed throughout the volume of the model, which purpose was to serve as validation points.

The model in pre-deformation and three deformed states is shown in Fig.10. The images were acquired at Emory University Hospital using a Siemens Magnetom Trio MRI 3 Tesla scanner with the following parameters: 256 x 256 x 72 voxels, voxel size 0.55 mm x 0.55 mm x 1.0 mm, TR = 2500 ms, TE = 4.4 ms, TI = 1100 ms, FOV = 140 mm, flip angle =

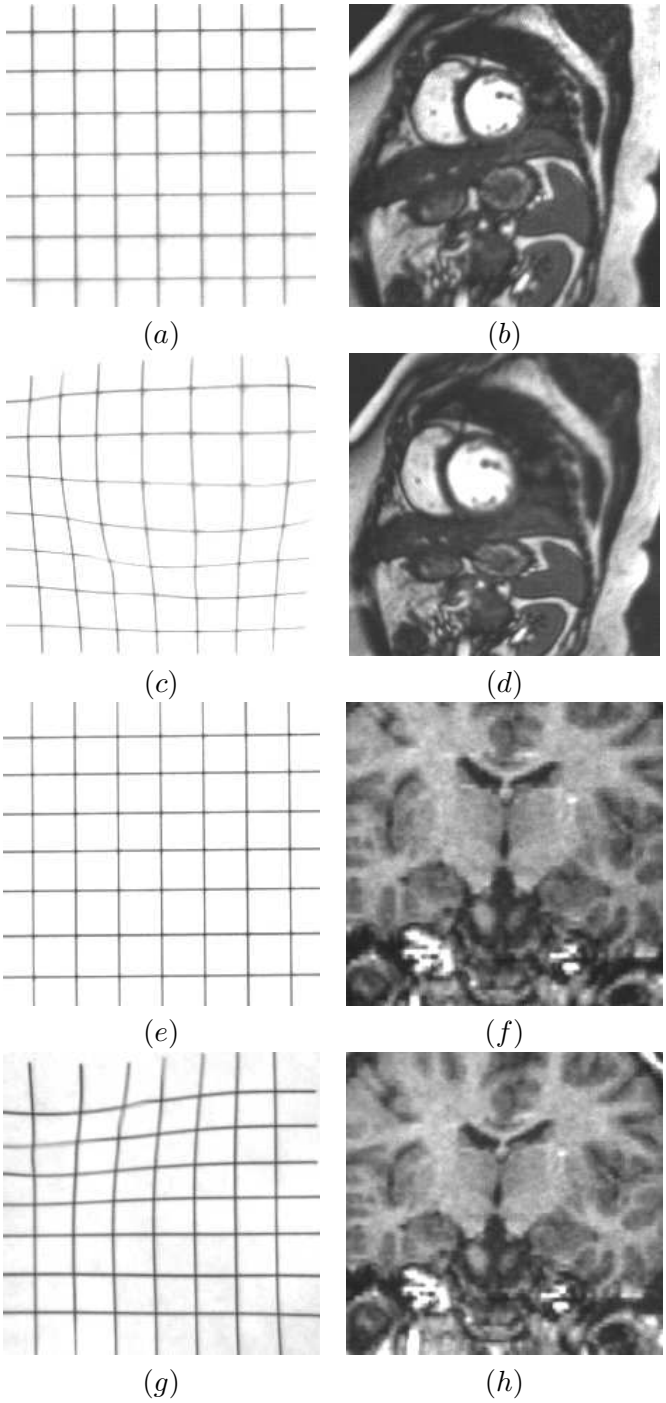

Figure 9: (a)(e) Undeformed grid images and (b)(f) undeformed medical images for two cases acquired by the CCD camera. Using an optical warper we can obtain (c)(g) deformed grid images and (d)(h) the correspondingly deformed medical images.

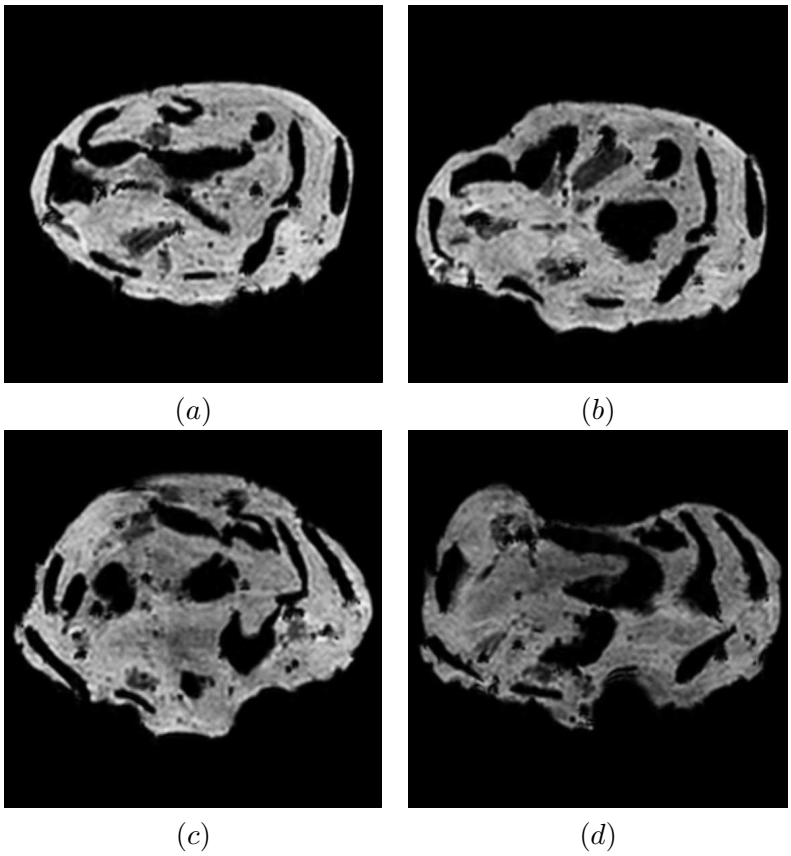

Figure 10: A section through the 3D MRI volume of the undeformed model (a), after first deformation (b), after second deformation (c), and after third deformation (d).

8 deg, 4 averages over signal acquisition.

We have developed a method for automated computation of the bead locations based on a template matching approach. The size of the beads was about 2 x 2 x 2 mm, which means that their location can be known with an accuracy of ± 1 mm in each direction.

Because the beads show up as clear dark voids in the images, they provide additional "artificial" strong image features for nonrigid image registration. In order to provide only "natural" image features we interpolated the surrounding voxel intensities over the bead voxels (Fig.11). Images with removed beads can be used to test 3D nonrigid image registration algorithms, while the bead locations can be used as validation points.

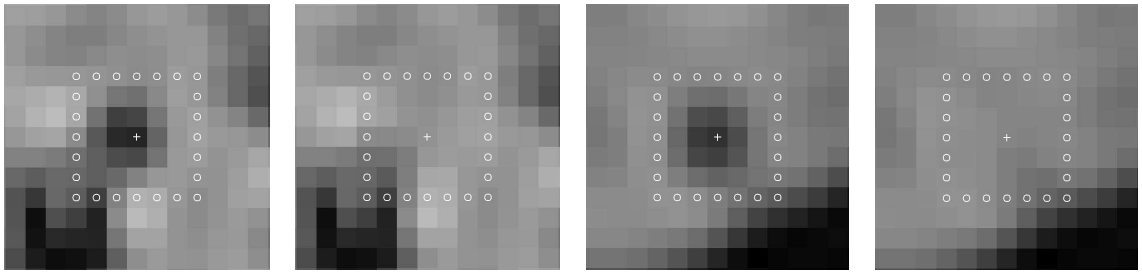

(a) (b) (c) (d)

Figure 11: A 2D section through a bead before (a) and after (b) bead removal by interpolation. Another bead removal example is shown in (c) and (d). The white circles represent the voxels used for interpolation of the bead voxels. The white cross represents the central bead voxel.

5.4 Manual Validation

The goal of this study was to assess the accuracy of manual validation and to analyze variability among observers. Five observers were asked, for 20 points in the undeformed image, to find the corresponding points in the deformed image. This was repeated for six 2D cases and one 3D case.

To test the reliability of the data provided by the observers, we removed one of the observers from the statistical analysis and the results didn't change significantly. This showed that the observers provided approximately equally accurate data.

CHAPTER 6

EXPERIMENTAL RESULTS

Three experiments are presented in this section to demonstrate how to implement the spline-based nonrigid image registration algorithms, how to achieve the transitivity and symmetric property when registering a sequence of images, and how to generate 2D and 3D validation data for nonrigid image registration algorithms.

6.1 Nonrigid image registration

The nonrigid registration algorithms were tested on pairs of simulated images with known deformations. The images were generated by deforming 2D and 3D MR images.

6.1.1 2D nonrigid registration

For 2D analysis, we have implemented the warping functions, thin-plate spline and cubic B-spline, and the image similarity measures, including mean square differences and normalized mutual information. All the combinations of the warping function and image similarity measure can easily be done. Here the registration algorithms were tested under two separate groups, the thin-plate spline with mean square differences and cubic B-spline with normalized mutual information. We used a T1 weighted coronal brain image and a short axis cardiac MR image as the object images, and artificially deformed these images to generate the target images with known displacement fields. We applied this method to generate 10 pairs of simulated data for testing the performance of the algorithm. Although these target images were artificially generated, the deformation patterns were controlled within a physically reasonable range. For the parameters set here, the initial value of the step size was 4 mm, and an initial control point spacing of 40 mm was chosen. After registration finished at the first level, the grid spacing was refined to 20 mm. Registration was then run again using the 20 mm grid and was refine to 10 mm at the final level, where the minimal value of the step size was 1 mm and only a few iterations were needed because of near-optimal

Table 1: The maximum error for 2D nonrigid image registration by thin-plate spline with mean squared differences. The unit for the displacements and errors is mm. The column of Maximum Disp. represents the maximum displacement between the target image and the object image.

Case	Maximum Disp.	Maximum error
1	7.6	2.49
2	10.5	2.82
3	6.86	1.41
4	8.50	2.56
5	7.30	2.31
6	8.97	1.58
7	10.03	2.01
8	6.90	1.48
9	7.57	1.66
10	9.19	1.72

initial condition.

Table 1 shows the registration error measured in terms of the maximal misregistration by running thin-plate spline warping function with the similarity measure of mean square difference over the brain images. The images have a size of 256 x 186 pixels and spatial resolution of 1 mm x 1.5 mm. Fig.12 shows one image pair from the simulated data together with the computed image and the displacement field. The red crosses in Fig.12(c) represent the deformation pattern, and the blue vectors and red vectors in Fig.12(d) represent true vector field and computed vector field respectively. Since the registration algorithm can effectively capture the deformations between the image pair, most of the true and the computed vectors overlap.

Table 2 shows another data set of the registration error by running cubic B-spline with normalized mutual information over the cardiac images. These cardiac images have have a size of 386 x 323 pixels and spatial resolution of 1 mm x 1 mm. Fig.13 shows one image pair together with the computed image and the displacement field.

6.1.2 3D nonrigid registration

For 3D analysis, the nonrigid registration algorithm was tested on 3D cardiac short axis MR images. An example of three orthogonal slices of these 3D images is shown in Fig. 14.

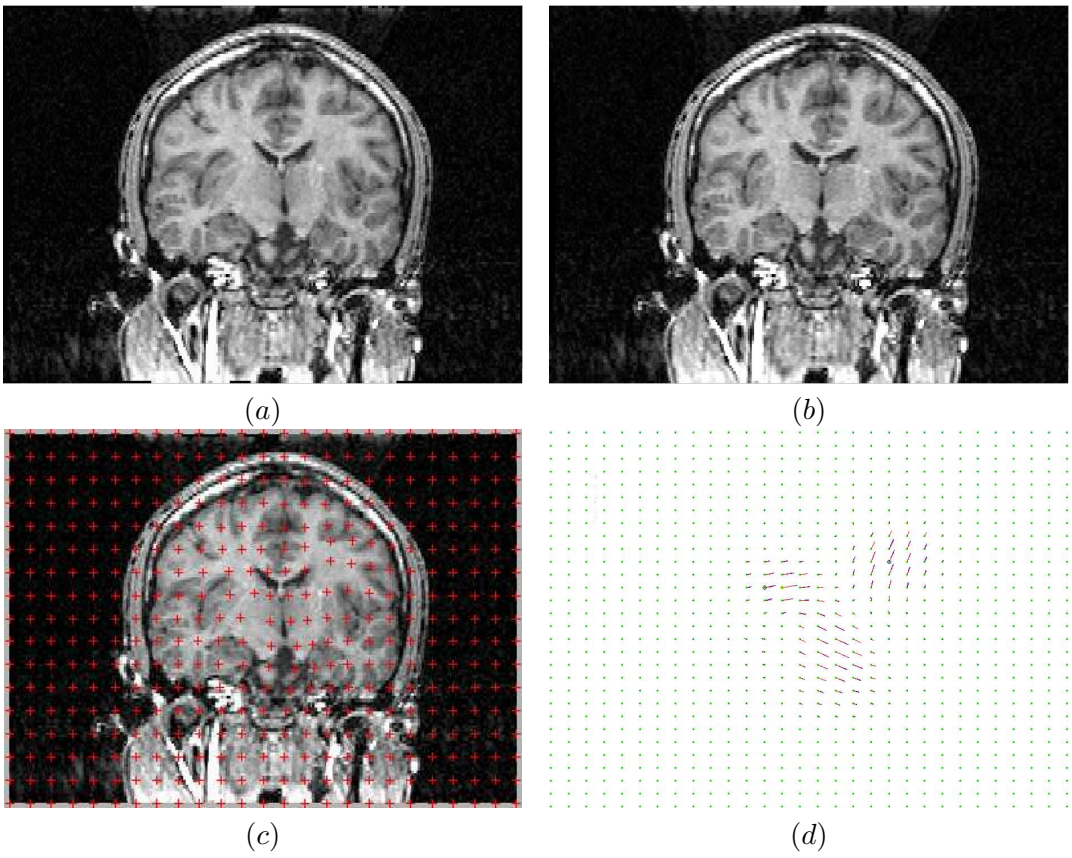

Figure 12: Nonrigid registration for 2D T1 weighted coronal brain images. (a) Target image (b) Object image (c) Computed image using thin-plate spline with mean square differences (d) Computed displacement field using thin-plate spline with mean square differences. The maximal error for this pair of images is 2.37 mm.

Table 2: The maximum error for 2D nonrigid image registration by cubic B-spline with normalized mutual information. The unit for the displacements and errors is mm. The column of Maximum Disp. represents the maximum displacement between the target image and the object image.

Case	Maximum Disp.	Maximum error
1	13.89	1.80
2	12.25	1.24
3	11.95	2.08
4	8.06	3.35
5	8.89	3.19
6	8.01	2.82
7	9.55	2.20
8	10.70	1.38
9	9.12	3.23
10	13.3	2.46

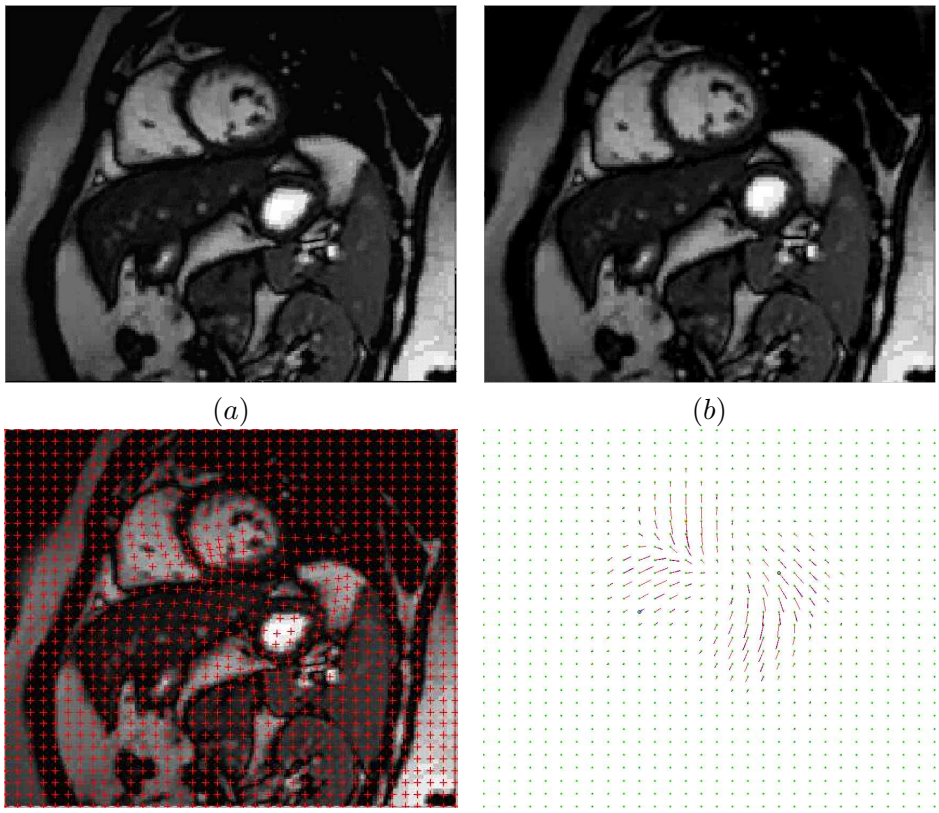

Figure 13: Nonrigid registration for 2D short axis MR cardiac images. (a) Target image (b) Object image (c) Computed image using cubic B-spline with normalized mutual information (d) Computed displacement field using cubic B-spline with normalized mutual information. The maximal error for this pair of images is 2.46 mm.

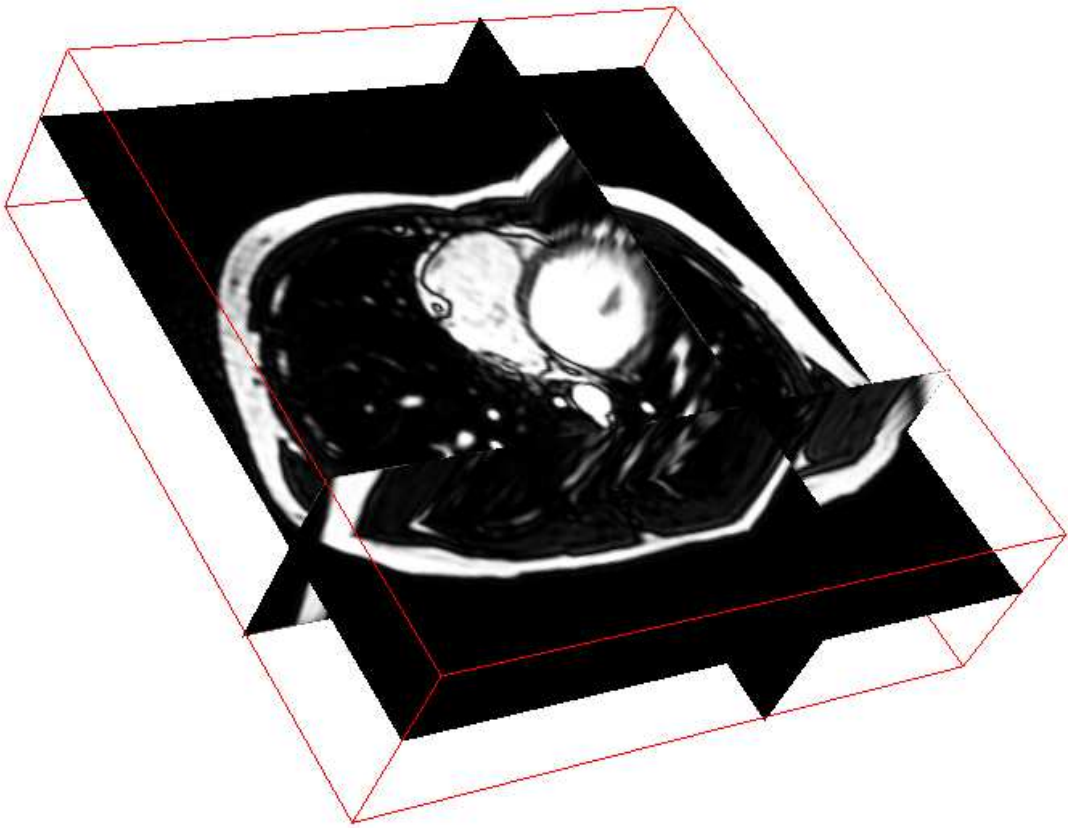

Figure 14: Three orthogonal slices of a 3D cardiac short axis MR image.

The images have a size of 256 x 256 x 20 voxels and spatial resolution of 1.328 mm x 1.328 mm x 5 mm. In this test, we applied the cubic B-spline warping method with the mean square difference as the image similarity measure, and set the 3-D grid spacing to be 20 mm and a multilevel step size from 10 mm to 5 mm and ended at 2.5 mm.

Table 3 summarized the registration accuracy of 9 simulated cases in terms of the maximum registration error. The experimental results have shown that the nonrigid image registration algorithm can efficiently recover the deformations. The range of the maximum displacement is from 10 mm to 30 mm and the maximum registration error is 5.09 mm, which is close to the voxel resolution 5 mm in z direction. The registration cannot perform better than the smallest voxel resolution of the image, because there is no more information available below this scale. Fig.15 and Fig.16 show two examples of the 3D nonrigid image registration.

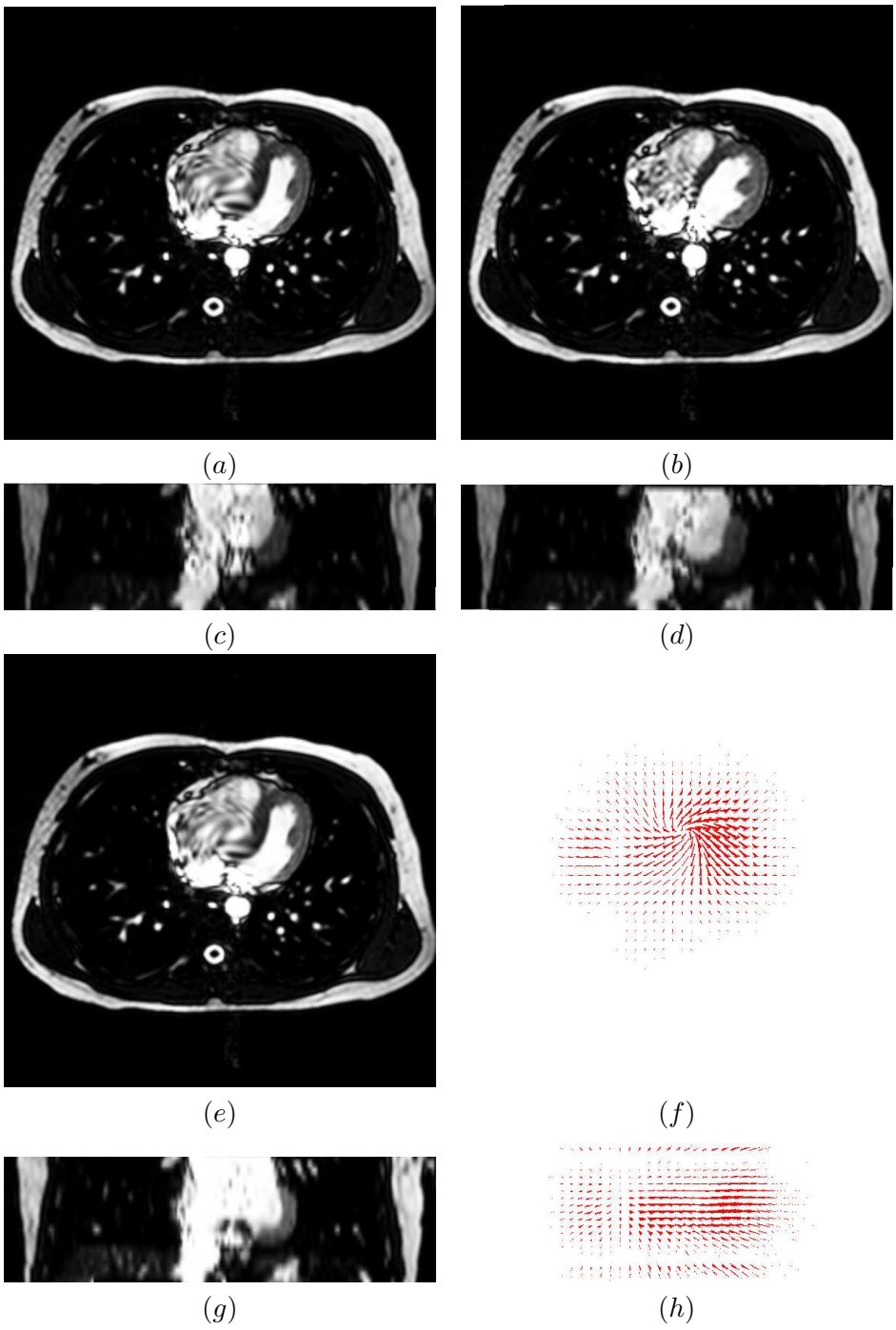

Figure 15: 3D nonrigid registration test for case 1. (a) one slice of the target image in xy plane (b) one slice of the object image in xy plane (c) one slice of the target image in yz plane (d) one slice of the object image in yz plane (e) one slice of the computed image in xy plane (f) the vector field in xy plane (g) one slice of the computed image in yz plane (h) the vector field in yz plane.

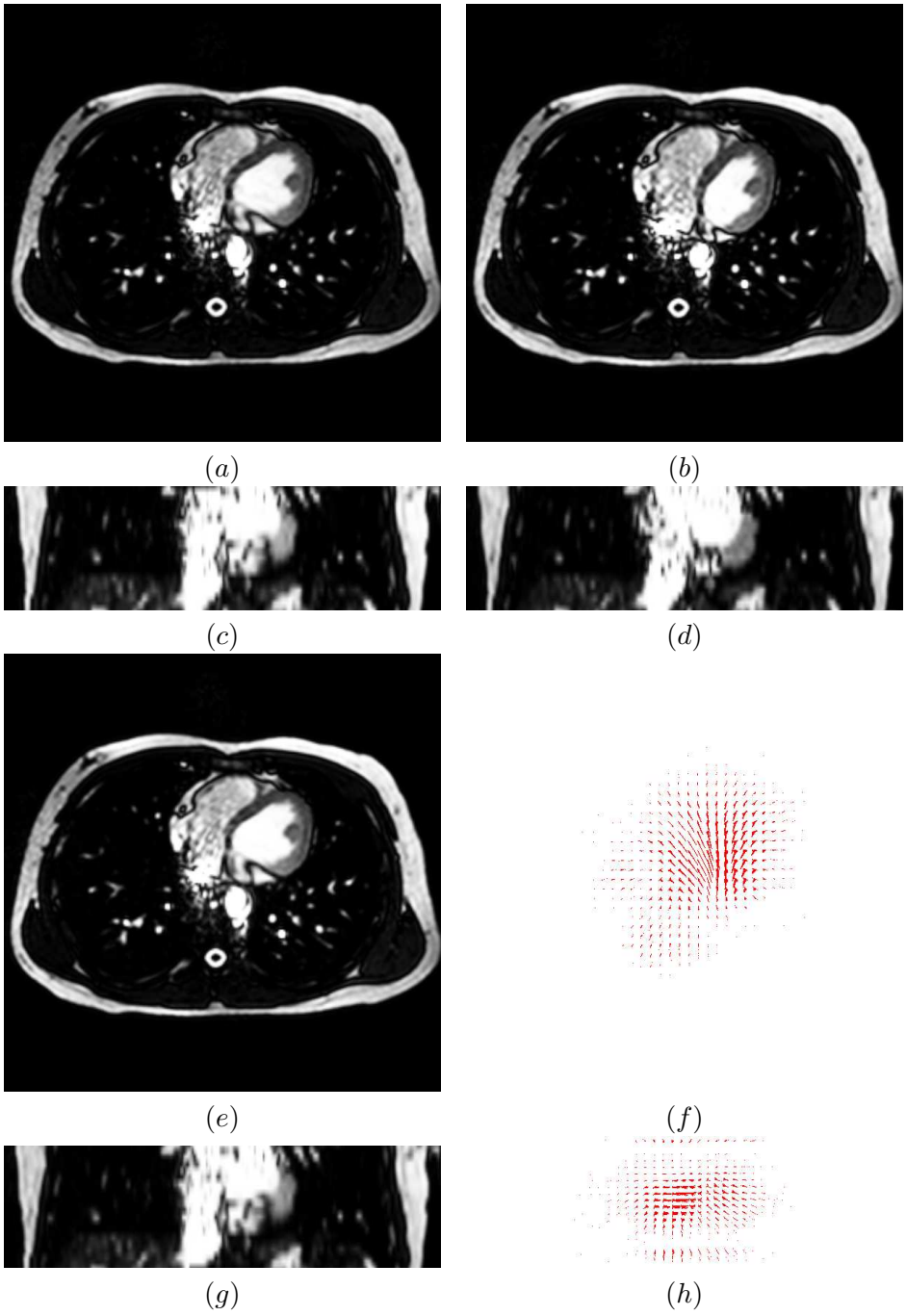

Figure 16: 3D nonrigid registration test for case 2. (a) one slice of the object image in xy plane (b) one slice of the target image in xy plane (c) one slice of the object image in yz plane (d) one slice of the target image in yz plane (e) one slice of the computed image in xy plane (f) the vector field in xy plane (g) one slice of the computed image in yz plane (h) the vector field in yz plane.

Table 3: The maximum error for 3D nonrigid image registration. The unit for the displacements and errors is mm. The column of Maximum Disp. represents the maximum displacement between the target image and the object image.

Case	Maximum Disp.	Maximum error
1	29.93	5.09
2	16.59	4.94
3	10.04	2.31
4	17.17	3.30
5	13.90	3.42
6	14.05	2.79
7	16.52	2.14
8	10.88	4.44
9	14.03	2.45

6.2 Transitivity

The transitivity analysis was performed on two 2-D and one 3-D MRI data set. The transformations between each pair of images were estimated using the multi-scale cubic B-spline-based nonrigid image registration algorithm. To validate the method, we have defined the transitivity error by comparing the identity transformation and the composition of the transformation from images I_1 to I_2, I_2 to I_3, and I_1 to I_3 as the mean (std, max) over all $r \, \epsilon \, \mathrm{D}$ of

$$e(r) = \|\mathrm{G}(I_2, I_3)(\mathrm{G}(I_1, I_2)(r)) - \mathrm{G}(I_1, I_3)(r)\| \tag{15}$$

with D being the domain of the transformation. In an ideal situation the error is zero.

6.2.1 2D transitivity

Tables 4 and 5 show the transitivity error for the 2D experiments. These tables show that the source of the transitivity error is from the error of computing the inverse transform $(\Gamma(I_2, M)^{-1})$. If the inverse function could be computed exactly, the transitivity error would be bound only by the machine precision. In these experiments, the transformations are represented by thin plate splines, which cannot be inverted analytically. Therefore, we computed the inverse transformation numerically, with a specified maximal error of 10^{-6} pixels. Note that this value is similar to the maximal transitivity error in Tables 4 and 5.

Table 4: The transitivity error (max, mean std) for random triples of images (I_1, I_2, I_3) with a given model (M) from the first sequence of 2D short axis cardiac MR images. The units for the errors are pixels (e.g. $1.0 \cdot 10^{-6}$ means a millionth part of a pixel). The columns I_1, I_2, I_3 and M represent respective image indexes from the image sequence.

I_1	I_2	I_3	M	max	mean	std
16	10	8	4	$2.0 \cdot 10^{-6}$	$9.1 \cdot 10^{-7}$	$1.5 \cdot 10^{-7}$
15	13	8	4	$2.1 \cdot 10^{-6}$	$8.7 \cdot 10^{-7}$	$1.4 \cdot 10^{-7}$
1	14	8	4	$2.0 \cdot 10^{-6}$	$8.7 \cdot 10^{-7}$	$1.3 \cdot 10^{-7}$
12	3	7	4	$1.5 \cdot 10^{-6}$	$8.6 \cdot 10^{-7}$	$1.2 \cdot 10^{-7}$
15	7	1	4	$1.6 \cdot 10^{-6}$	$8.6 \cdot 10^{-7}$	$1.0 \cdot 10^{-7}$
6	14	1	4	$1.8 \cdot 10^{-6}$	$8.8 \cdot 10^{-7}$	$1.2 \cdot 10^{-7}$
3	10	5	4	$1.3 \cdot 10^{-6}$	$8.8 \cdot 10^{-7}$	$8.8 \cdot 10^{-7}$
1	12	8	4	$2.1 \cdot 10^{-6}$	$9.0 \cdot 10^{-7}$	$1.4 \cdot 10^{-7}$
15	8	7	4	$1.7 \cdot 10^{-6}$	$9.0 \cdot 10^{-7}$	$1.3 \cdot 10^{-7}$

We have repeated the experiments with the maximal error for the inverse transform set to 10^{-4} pixels, and the maximal transitivity error was about 10^{-4} pixels, which confirms that the error of numerical computation of the inverse transform directly affects the transitivity error.

Fig.17 and Fig.18 show two triples of images randomly selected from the two sequences of 2D cardiac images together with corresponding transformations computed by the presented method.

6.2.2 3D transitivity

For 3-D analysis, the maximal error for the inverse transform was set to 10^{-4} voxels. Table 6 shows the transitivity error for the 3D experiments. The same as the 2-D analysis, the error of numerical computation of the inverse transform directly affects the transitivity error.

Fig.19 and Fig.20 show two triples of images randomly selected from the a sequences of 3D cardiac images together with corresponding transformations computed by the presented method.

6.3 Symmetry

Symmetry is a desired property for the image registration algorithms. Without symmetry, the forward transformation would define one correspondence between the image pairs while

Table 5: The transitivity error (max, mean std) for random triples of images (I_1, I_2, I_3) with a given model (M) from the second sequence of 2D short axis cardiac MR images. The units for the errors are pixels (e.g. $1.0 \cdot 10^{-6}$ means a millionth part of a pixel). The columns I_1, I_2, I_3 and M represent respective image indexes from the image sequence.

I_1	I_2	I_3	M	max	mean	std
8	10	14	6	$6.0 \cdot 10^{-6}$	$9.6 \cdot 10^{-7}$	$2.4 \cdot 10^{-7}$
8	9	4	6	$4.0 \cdot 10^{-6}$	$9.3 \cdot 10^{-7}$	$2.0 \cdot 10^{-7}$
8	13	5	6	$2.5 \cdot 10^{-6}$	$9.6 \cdot 10^{-7}$	$1.3 \cdot 10^{-7}$
3	4	11	6	$6.3 \cdot 10^{-6}$	$9.6 \cdot 10^{-7}$	$2.2 \cdot 10^{-7}$
11	7	10	6	$2.9 \cdot 10^{-6}$	$9.7 \cdot 10^{-7}$	$1.8 \cdot 10^{-7}$
11	13	12	6	$4.7 \cdot 10^{-6}$	$9.9 \cdot 10^{-7}$	$2.0 \cdot 10^{-7}$
2	8	7	6	$8.6 \cdot 10^{-6}$	$9.5 \cdot 10^{-7}$	$1.6 \cdot 10^{-7}$
3	12	13	6	$9.0 \cdot 10^{-6}$	$1.0 \cdot 10^{-7}$	$3.3 \cdot 10^{-7}$
9	10	3	6	$6.2 \cdot 10^{-6}$	$9.6 \cdot 10^{-7}$	$2.5 \cdot 10^{-7}$

Table 6: The transitivity error (max, mean std) for random triples of images (I_1, I_2, I_3) with a given model (M) from the 3D short axis cardiac MR images. The units for the errors are voxels. The columns I_1, I_2, I_3 and M represent respective image indexes from the image sequence.

I_1	I_2	I_3	M	max	mean	std
3	13	5	8	$2.2 \cdot 10^{-4}$	$2.1 \cdot 10^{-5}$	$3.7 \cdot 10^{-5}$
7	14	3	13	$1.1 \cdot 10^{-4}$	$1.9 \cdot 10^{-5}$	$3.4 \cdot 10^{-5}$
16	14	5	6	$1.2 \cdot 10^{-4}$	$2.1 \cdot 10^{-5}$	$3.5 \cdot 10^{-5}$
12	7	16	13	$1.3 \cdot 10^{-4}$	$2.1 \cdot 10^{-5}$	$3.6 \cdot 10^{-5}$
15	5	8	7	$1.1 \cdot 10^{-4}$	$2.1 \cdot 10^{-5}$	$3.5 \cdot 10^{-5}$
5	7	16	4	$1.4 \cdot 10^{-4}$	$2.1 \cdot 10^{-5}$	$3.5 \cdot 10^{-5}$
4	6	12	15	$2.0 \cdot 10^{-4}$	$2.2 \cdot 10^{-5}$	$3.7 \cdot 10^{-5}$
2	1	11	9	$1.4 \cdot 10^{-4}$	$2.1 \cdot 10^{-5}$	$3.6 \cdot 10^{-5}$

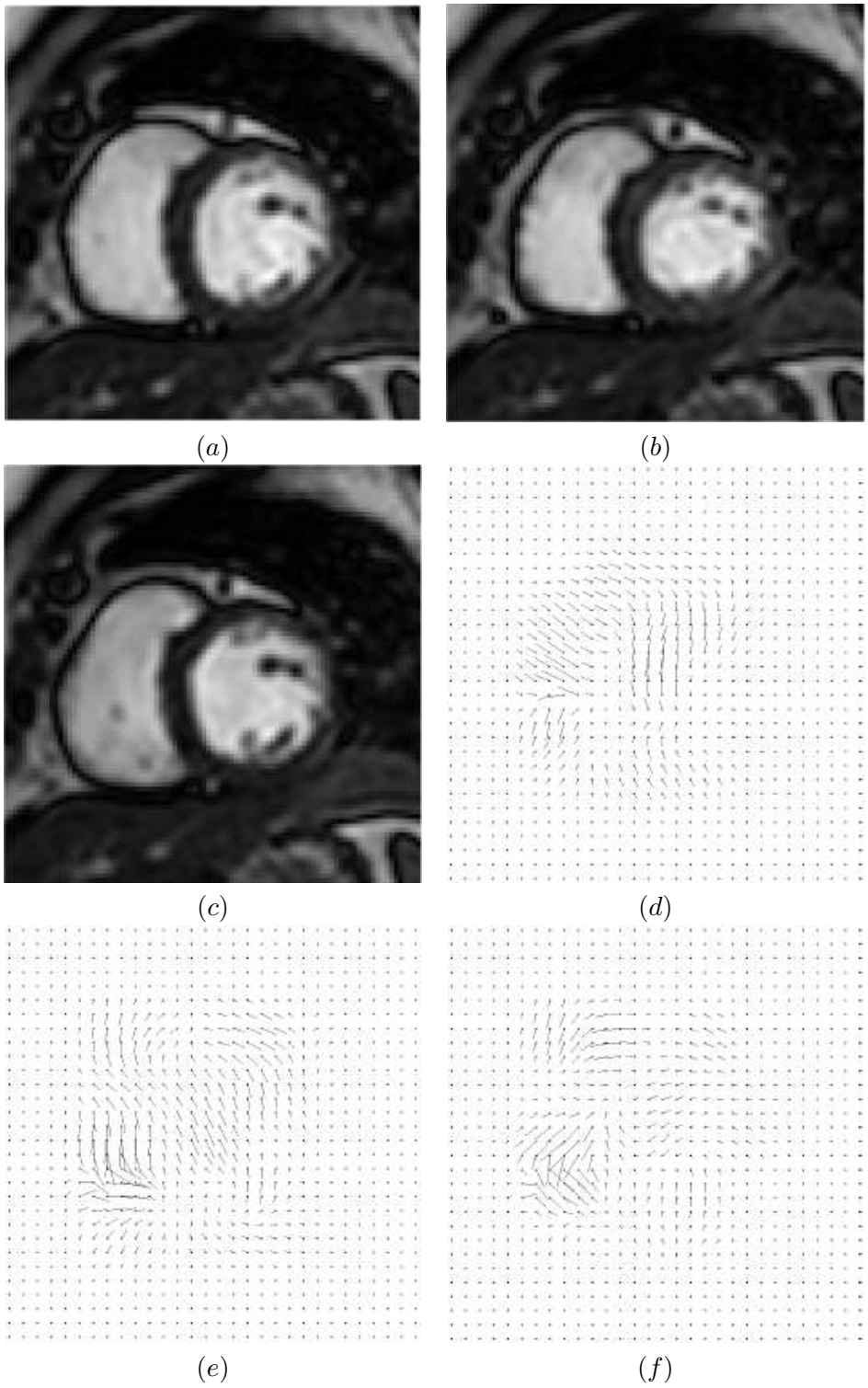

Figure 17: 2D transitivity test for case 1. Three randomly selected images from a sequence of short axis 2D cardiac MR images are shown in (a), (b), and (c). The computed displacement field from (a) to image (b) is shown in (d), the computed displacement field from image (b) to image (c) is shown in (e), and the computed displacement field from image (a) to image (c) is shown in (f). The mean (max) transitivity error for this triple of images is $1.0 \cdot 10^{-6}(9.0 \cdot 10^{-6})$pixels.

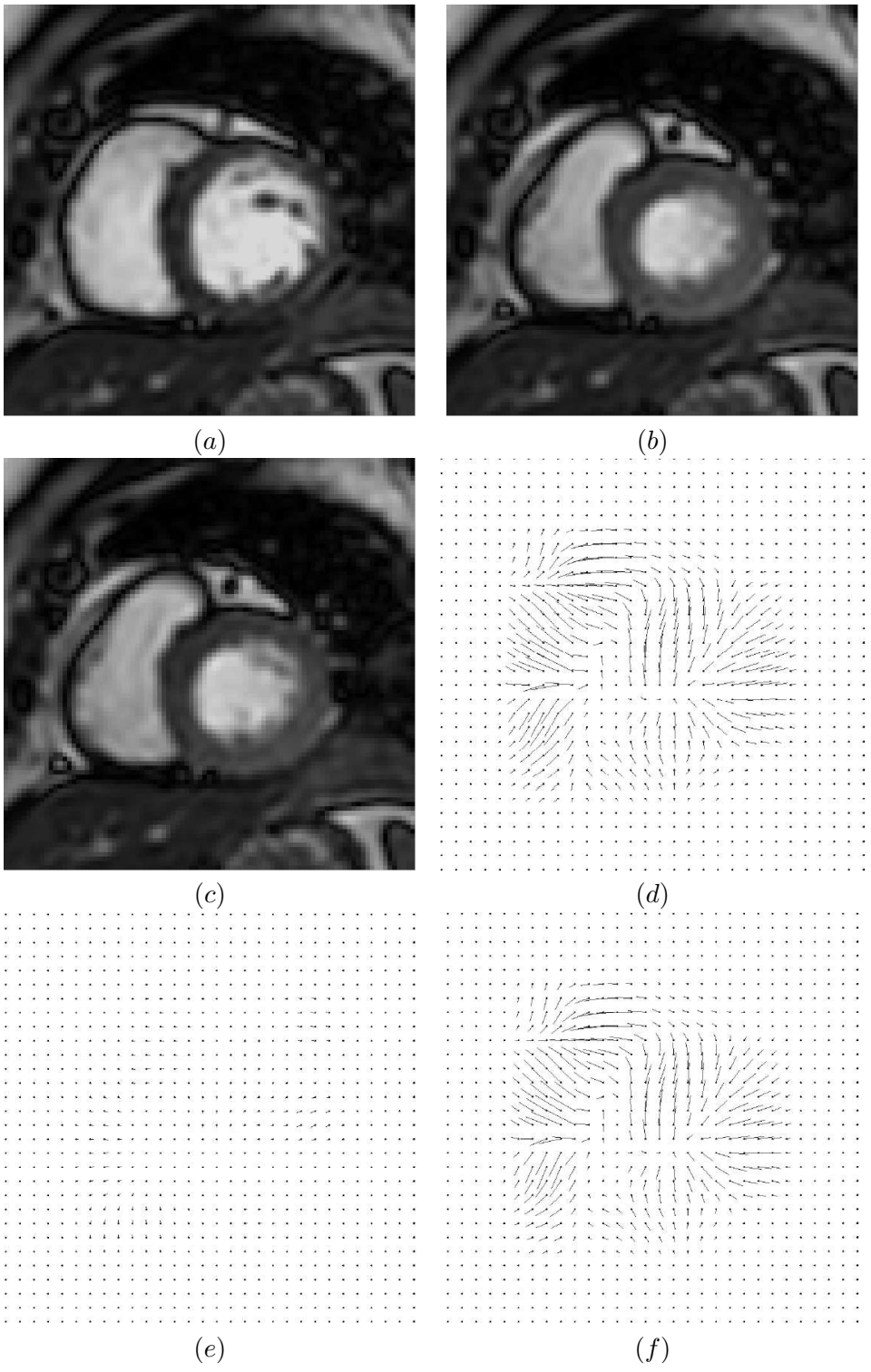

Figure 18: 2D transitivity test for case 2. Three randomly selected images from a sequence of short axis 2D cardiac MR images are shown in (a), (b), and (c). The computed displacement field from (a) to image (b) is shown in (d), the computed displacement field from image (b) to image (c) is shown in (e), and the computed displacement field from image (a) to image (c) is shown in (f). The mean (max) transitivity error for this triple of images is $9.0 \cdot 10^{-7}(1.7 \cdot 10^{-6})$pixels.

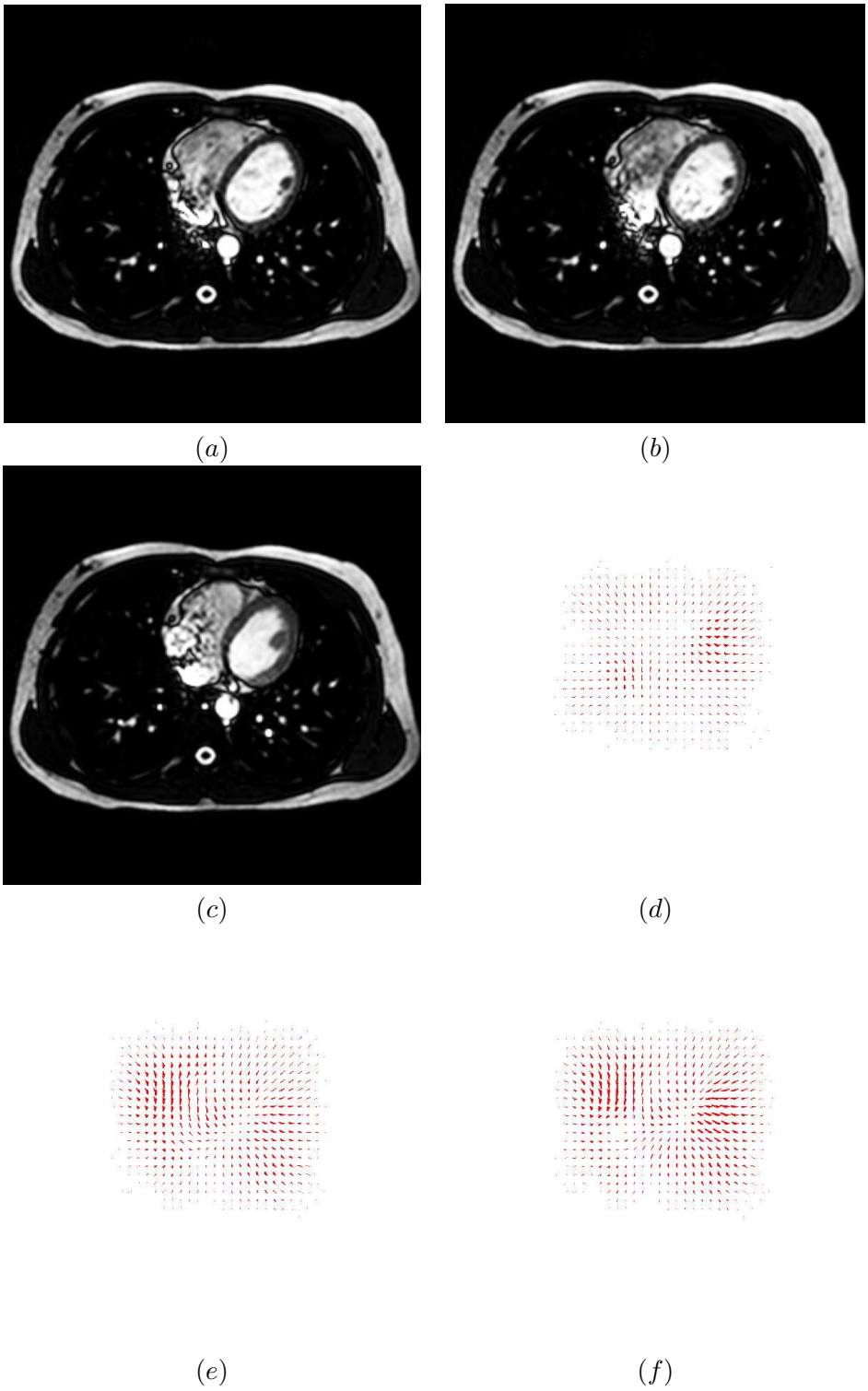

Figure 19: 3D transitivity test for case 1. Three randomly selected images from a sequence of short axis 3D cardiac MR images are shown in (a), (b), and (c). The computed displacement field from (a) to image (b) is shown in (d), the computed displacement field from image (b) to image (c) is shown in (e), and the computed displacement field from image (a) to image (c) is shown in (f). The mean (max) transitivity error for this triple of images is $1.2 \cdot 10^{-4}(2.1 \cdot 10^{-5})$voxels.

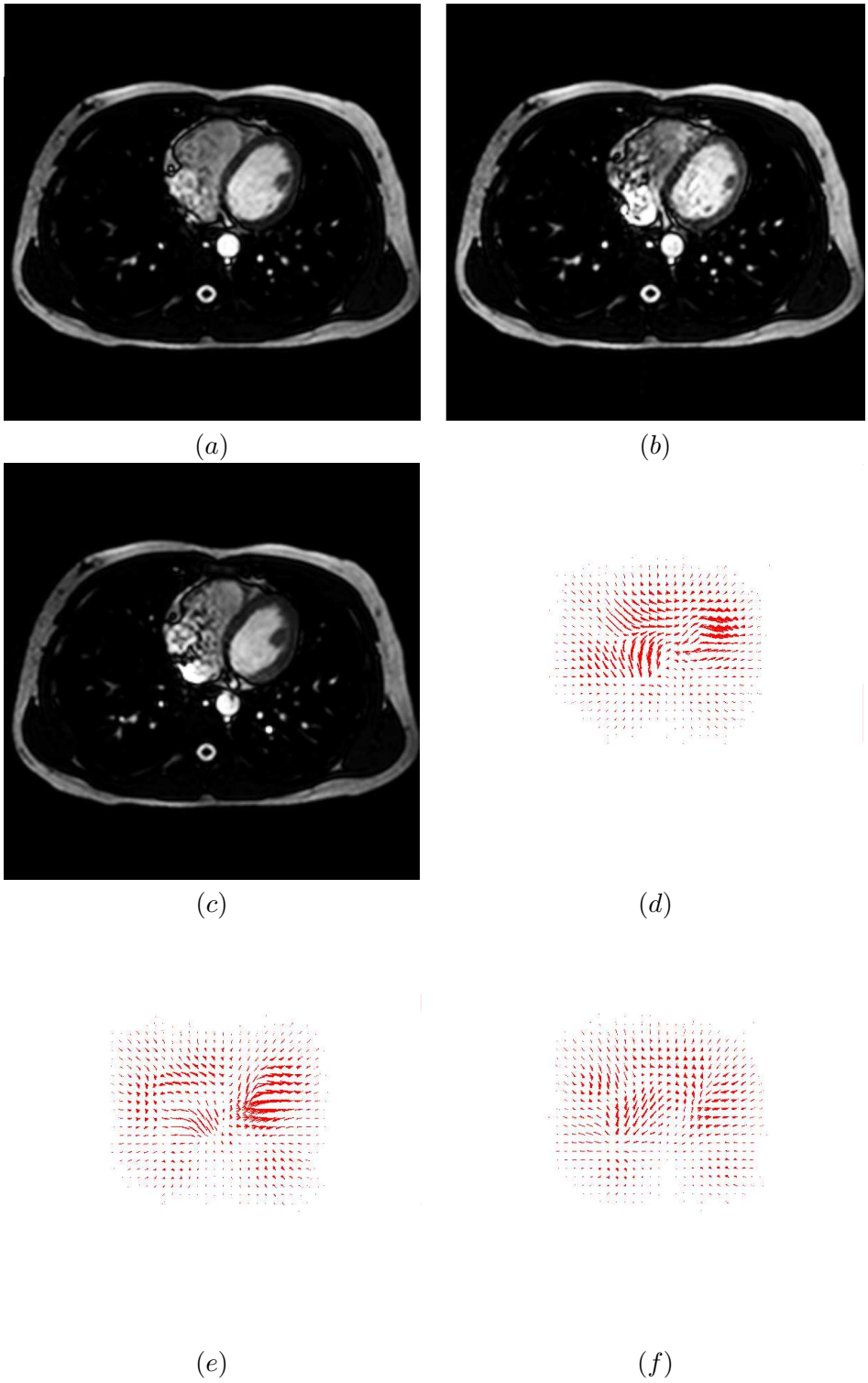

Figure 20: 3D transitivity test for case 2. Three randomly selected images from a sequence of short axis 3D cardiac MR images are shown in (a), (b), and (c). The computed displacement field from (a) to image (b) is shown in (d), the computed displacement field from image (b) to image (c) is shown in (e), and the computed displacement field from image (a) to image (c) is shown in (f). The mean (max) transitivity error for this triple of images is $1.2 \cdot 10^{-4}(2.1 \cdot 10^{-5})$voxels.

the reverse transformation would define a different correspondence. For the 2D and 3D symmetric analysis, we used the same registration algorithms, the same sequences of cardiac short axis MR images and set the same maximal error for the inverse transforms as in the transitive analysis. To quantitatively validate this approach, we have defined the symmetry error by comparing the composition of forward transformation from images I_1 to I_2, and reverse transformation from images I_2 to I_1 to the identity transformation as the mean (std, max) over all $r \, \epsilon \, \mathrm{D}$ of

$$e(r) = \|\mathrm{G}(I_2, I_1)(\mathrm{G}(I_1, I_2)(r)) - r\| \tag{16}$$

with D being the domain of the transformation. In an ideal situation the error will be zero.

6.3.1 2D symmetry

Tables 7 and 8 show the symmetry error for the 2D experiments. These tables show that the source of the symmetry error is from the error of computing the inverse transform $(\Gamma(I_2, M)^{-1})$. If the inverse function could be computed exactly, the symmetry error would be bound only by the machine precision.

Fig.21 and Fig.22 show two pairs of images randomly selected from the two sequences of 2D cardiac images together with corresponding transformations computed by the presented method.

6.3.2 3D symmetry

Table 9 shows the symmetry error for the 3D experiments. The same as in the 2-D analysis, the error of numerical computation of the inverse transform directly affects the transitivity error.

Fig.23 and Fig.24 show two pairs of images randomly selected from the a sequences of 3D cardiac images together with corresponding transformations and displacement field computed by the presented method.

Table 7: The symmetry error(max, mean std) for random pair of images (I_1, I_2) with a given model (M) from the first sequence of 2D short axis cardiac MR images. The units for the errors are pixels (e.g. $1.0 \cdot 10^{-6}$ means a millionth part of a pixel). The columns I_1, I_2 and M represent respective image indexes from the image sequence.

I_1	I_2	M	max	mean	std
16	11	6	$3.7 \cdot 10^{-6}$	$8.8 \cdot 10^{-7}$	$6.2 \cdot 10^{-7}$
8	1	6	$2.4 \cdot 10^{-6}$	$1.0 \cdot 10^{-6}$	$6.0 \cdot 10^{-7}$
8	10	6	$2.6 \cdot 10^{-6}$	$1.7 \cdot 10^{-6}$	$3.1 \cdot 10^{-7}$
15	12	6	$3.8 \cdot 10^{-6}$	$9.7 \cdot 10^{-7}$	$6.4 \cdot 10^{-7}$
7	15	6	$2.3 \cdot 10^{-6}$	$8.5 \cdot 10^{-7}$	$5.7 \cdot 10^{-7}$
15	1	6	$4.8 \cdot 10^{-6}$	$1.8 \cdot 10^{-6}$	$5.8 \cdot 10^{-7}$
4	10	6	$2.0 \cdot 10^{-6}$	$7.4 \cdot 10^{-7}$	$4.7 \cdot 10^{-7}$
4	1	6	$3.4 \cdot 10^{-6}$	$1.6 \cdot 10^{-6}$	$5.0 \cdot 10^{-7}$
8	15	6	$2.5 \cdot 10^{-6}$	$9.1 \cdot 10^{-7}$	$6.2 \cdot 10^{-7}$
14	9	6	$3.9 \cdot 10^{-6}$	$8.5 \cdot 10^{-7}$	$5.9 \cdot 10^{-7}$

Table 8: The symmetry error(max, mean std) for random pair of images (I_1, I_2) with a given model (M) from the second sequence of 2D short axis cardiac MR images. The units for the errors are pixels (e.g. $1.0 \cdot 10^{-6}$ means a millionth part of a pixel). The columns I_1, I_2 and M represent respective image indexes from the image sequence.

I_1	I_2	M	max	mean	std
14	1	11	$6.1 \cdot 10^{-6}$	$1.7 \cdot 10^{-6}$	$5.8 \cdot 10^{-7}$
14	9	11	$3.9 \cdot 10^{-6}$	$8.5 \cdot 10^{-7}$	$5.6 \cdot 10^{-7}$
7	5	11	$2.2 \cdot 10^{-6}$	$4.9 \cdot 10^{-7}$	$6.5 \cdot 10^{-7}$
4	5	11	$3.3 \cdot 10^{-6}$	$1.8 \cdot 10^{-6}$	$3.7 \cdot 10^{-7}$
3	12	11	$4.8 \cdot 10^{-6}$	$7.9 \cdot 10^{-7}$	$5.9 \cdot 10^{-7}$
14	10	11	$3.9 \cdot 10^{-6}$	$9.3 \cdot 10^{-7}$	$6.0 \cdot 10^{-7}$
15	14	11	$5.0 \cdot 10^{-6}$	$1.9 \cdot 10^{-6}$	$5.3 \cdot 10^{-7}$
5	6	11	$1.3 \cdot 10^{-6}$	$9.5 \cdot 10^{-7}$	$6.3 \cdot 10^{-8}$
12	5	11	$3.6 \cdot 10^{-6}$	$7.9 \cdot 10^{-7}$	$5.7 \cdot 10^{-7}$
10	6	11	$1.7 \cdot 10^{-6}$	$9.7 \cdot 10^{-7}$	$1.2 \cdot 10^{-7}$

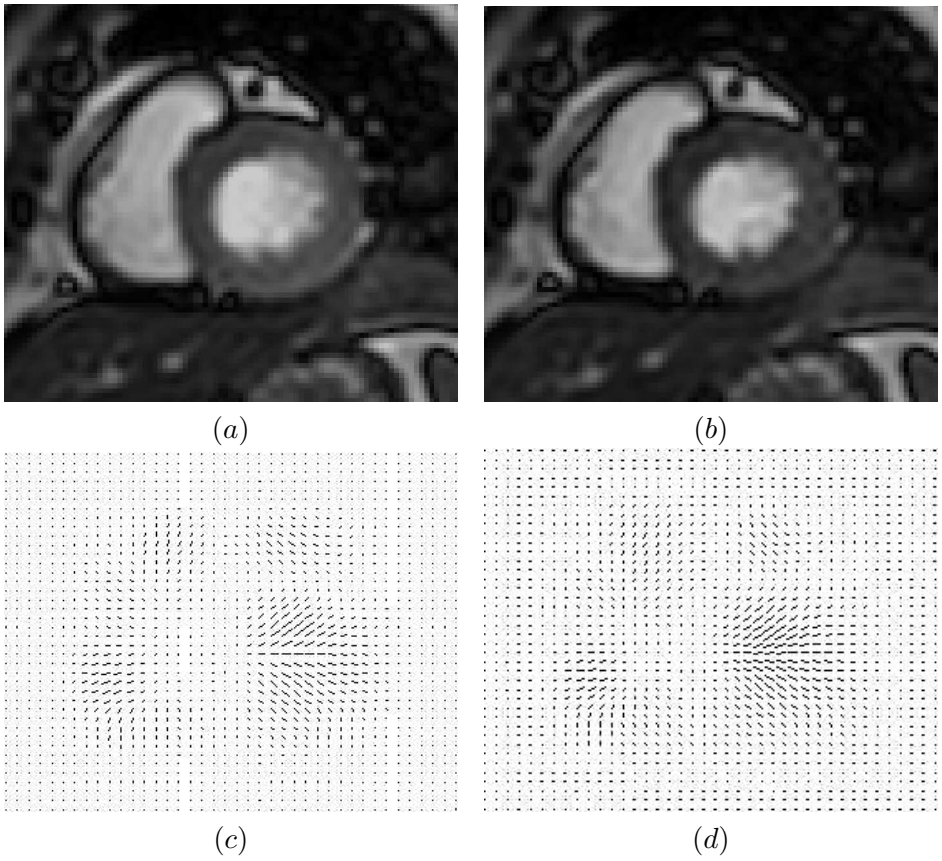

Figure 21: 2D symmetry test for case 1. Two randomly selected images from a sequence of short axis 2D cardiac MR images are shown in (a) and (b). The computed displacement field from (a) to image (b) is shown in (c), the computed displacement field from image (b) to image (a) is shown in (d). The mean (max) symmetry error for this triple of images is $1.3 \cdot 10^{-6}(6.1 \cdot 10^{-6})$pixels.

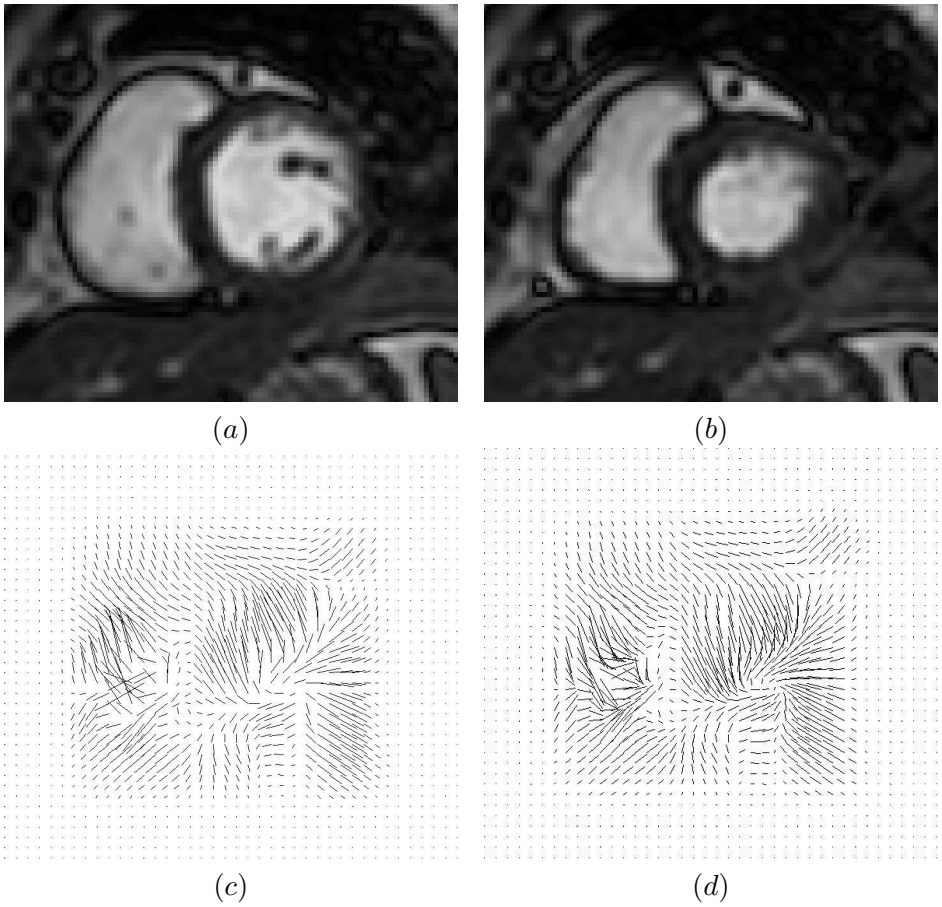

Figure 22: 2D symmetry test for case 2. Two randomly selected images from a sequence of short axis 2D cardiac MR images are shown in (a) and (b). The computed displacement field from (a) to image (b) is shown in (c), the computed displacement field from image (b) to image (a) is shown in (d). The mean (max) symmetry error for this triple of images is $7.9 \cdot 10^{-7}(4.8 \cdot 10^{-6})$pixels.

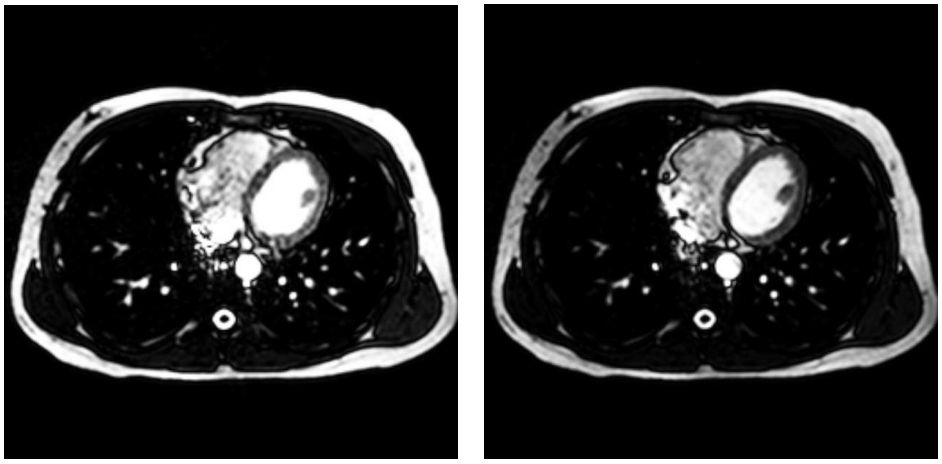

(*a*) (*b*)

(*c*) (*d*)

Figure 23: 3D symmetry test for case 1. Two randomly selected images from a sequence of short axis 2D cardiac MR images are shown in (a) and (b). The computed displacement field from (a) to image (b) is shown in (c), the computed displacement field from image (b) to image (a) is shown in (d). The mean (max) symmetry error for this triple of images is $7.9 \cdot 10^{-7}(4.8 \cdot 10^{-6})$pixels.

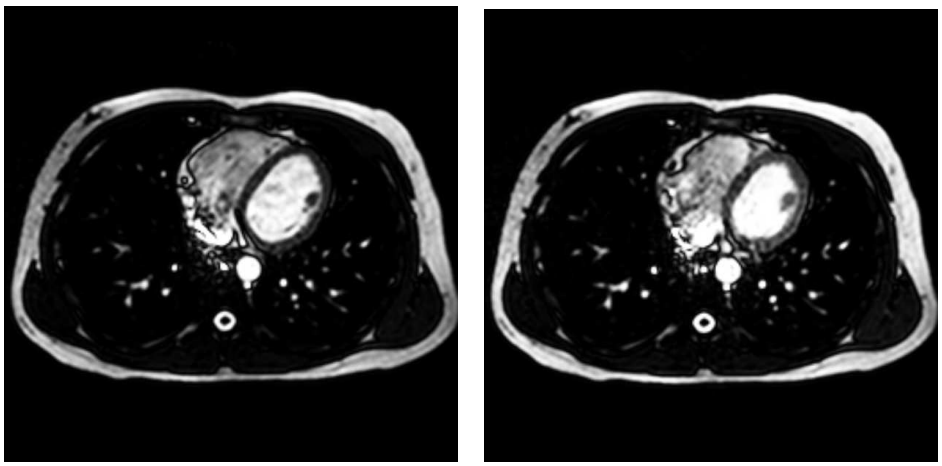

(a) (b)

(c) (d)

Figure 24: 3D symmetry test for case 2. Two randomly selected images from a sequence of short axis 2D cardiac MR images are shown in (a) and (b). The computed displacement field from (a) to image (b) is shown in (c), the computed displacement field from image (b) to image (a) is shown in (d). The mean (max) symmetry error for this triple of images is $7.9 \cdot 10^{-7}(4.8 \cdot 10^{-6})$pixels.

Table 9: The symmetry error(max, mean std) for random pair of images (I_1, I_2) with a given model (M) from the second sequence of 2D short axis cardiac MR images. The units for the errors are pixels (e.g. $1.0 \cdot 10^{-6}$ means a millionth part of a pixel). The columns I_1, I_2 and M represent respective image indexes from the image sequence.

I_1	I_2	M	max	mean	std
10	5	8	$1.8 \cdot 10^{-4}$	$2.5 \cdot 10^{-5}$	$4.9 \cdot 10^{-5}$
12	4	6	$2.9 \cdot 10^{-4}$	$2.9 \cdot 10^{-5}$	$5.3 \cdot 10^{-5}$
14	12	5	$2.2 \cdot 10^{-4}$	$2.9 \cdot 10^{-5}$	$5.4 \cdot 10^{-5}$
8	11	4	$2.8 \cdot 10^{-4}$	$3.8 \cdot 10^{-5}$	$6.6 \cdot 10^{-5}$
4	14	12	$4.1 \cdot 10^{-4}$	$3.0 \cdot 10^{-5}$	$5.5 \cdot 10^{-5}$
5	3	7	$2.8 \cdot 10^{-4}$	$3.5 \cdot 10^{-5}$	$6.2 \cdot 10^{-5}$
16	6	13	$2.3 \cdot 10^{-4}$	$2.7 \cdot 10^{-5}$	$5.0 \cdot 10^{-5}$
10	2	5	$2.3 \cdot 10^{-4}$	$2.5 \cdot 10^{-5}$	$4.7 \cdot 10^{-5}$
8	13	3	$6.5 \cdot 10^{-4}$	$3.3 \cdot 10^{-5}$	$6.2 \cdot 10^{-5}$
9	2	6	$5.6 \cdot 10^{-4}$	$2.5 \cdot 10^{-5}$	$4.8 \cdot 10^{-5}$

6.4 New Validation Strategies

6.4.1 2D validation strategy

For the 2D cases presented in this research, we used one cardiac MR short axis image slices and one brain MR coronal image slice. By applying the optical warper in different ways we generated three different deformations patterns for each image, thus producing a total of six cases. We ran the method described in Section 5.2 on the six cases using grids with 7 by 7 lines, i.e. with 49 line intersections. As described above, the accuracy of the method is 1 pixel. Fig.25 shows one of the six cases generated by the automated method.

For the manual validation, to decrease the load on the observers, we randomly selected 20 out of 49 markers for each of the six cases. The observers were presented with the selected markers in the undeformed images and were asked to find the corresponding points in the deformed images. Thus, each observer extracted a total of 120 markers. For each marker, the outputs of the five observers were averaged and standard deviation was computed. For each point in the undeformed image a mean and std (over the points in the deformed image set by the five observers) were computed. The means were compared against the result of the automated method (which output is within 1 pixel from the true values; clearly, the true values are not know).

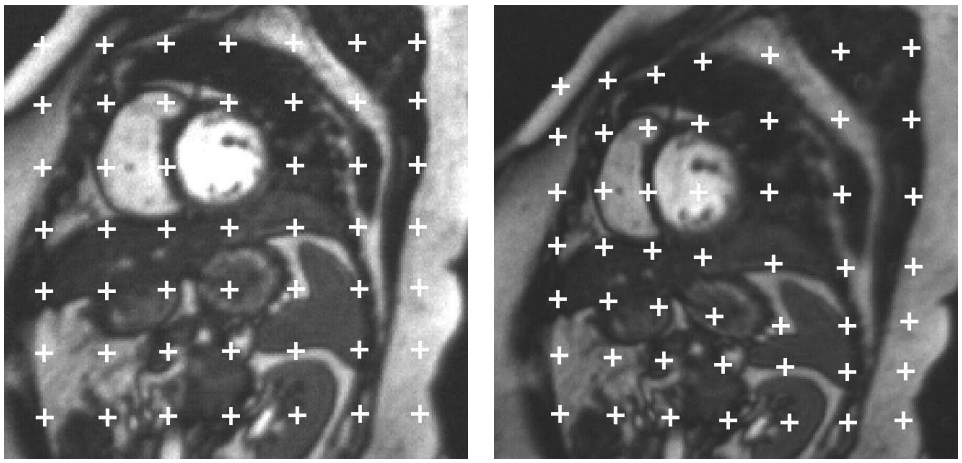

Figure 25: A pair of images (left - undeformed image, right - deformed image) and a set of corresponding points displayed over the images were generated by the automated method. The accuracy of the data is 1 pixel, i.e. the locations of points in the deformed image are not more than a pixel away from the true locations. This data can be used for validation of nonrigid image registration algorithms.

In Table 10, we listed the average error for the five observers in x direction, e_x, y direction, e_y, and error magnitude, $\|\boldsymbol{e}\|$, over the twenty markers for case 2. The errors are differences between the means over the five observers and the output of the automated method (which for this purpose can be considered "true" data since its accuracy is known). Additionally, the standard deviation, Std, of the five observers and the displacement, Disp, between the "true" points in the two images are given in the same table. All values are in pixels. Table 11 was generated using the same statistical analysis as in Table 10, but only the mean and maximum value over the twenty markers for cases 1 to 6 are given. In all cases, the maximal displacements are between 11 and 22 pixels. The mean error magnitudes are between 0.6 and 1.4 pixel, but the maximal error is up to 5.4 pixel in case 3. For markers located in homogeneous regions, it was difficult for the observers to set the corresponding points due to a lack of image features. For this reason, we manually selected markers located at stronger image features. The results of the same statistical analysis done on these markers for cases 1 to 6 are shown in Table 12. Now the maximal error magnitude is down to 2.0 pixel and the mean errors are between 0.6 and 1.0 pixel. Fig. 26 (a) is the plot of the standard deviation versus error magnitude for case 2. From the plot it seems

Table 10: The average error for five observers in x direction, e_x, y direction, e_y, error magnitude, $\|\boldsymbol{e}\|$, standard deviation, Std and displacement, Disp, for twenty markers for case 2. All values are in pixels.

Marker	e_x	e_y	$\|\boldsymbol{e}\|$	**Std**	**Disp**
1	0.8	-0.4	0.9	0.2	7.4
2	0.3	-0.8	0.9	0.7	4.1
3	1.0	0.0	1.0	0.8	10.3
4	0.9	-0.3	0.9	1.8	10.0
5	0.9	-0.0	0.8	0.5	3.5
6	-0.3	-0.8	0.8	0.5	5.6
7	0.0	-0.3	0.3	0.3	10.5
8	-0.3	1.1	1.2	0.8	17.5
9	-2.6	0.1	2.6	1.0	5.0
10	0.7	0.0	0.7	0.4	1.1
11	0.2	0.1	0.2	0.5	3.4
12	-0.9	-1.3	1.6	1.8	17.5
13	0.4	-0.8	0.9	0.9	18.8
14	-1.0	-1.0	1.4	1.5	10.5
15	3.0	3.0	4.2	1.9	13.6
16	1.3	0.3	1.4	3.2	14.5
17	1.2	-1.3	1.7	1.0	7.6
18	1.2	-1.5	1.9	0.8	4.9
19	0.0	-0.7	0.7	0.9	14.8
20	0.8	-0.6	1.0	0.6	21.4
mean	0.4	-0.3	1.3	1.0	10.1
max	3.0	3.0	4.2	3.2	21.4

that there exists some correlation between the two variables. The correlation coefficients of all six cases are listed in Table 13. In case 1, the correlation coefficient is almost equal to zero, which means that practically there is no relationship between the two variables. The correlation coefficient values from Table 13 indicate that the standard deviation is not a reliable measure of the error for individual points. However, when the standard deviation is averaged over all the points in one image then it becomes highly correlated with the mean error. A plot of the average std (averaged over all the points in one image) versus the mean error is given in Fig. 26 (b). The six points in the plot correspond to the six cases. The correlation coefficient between the two variables is .95 for this situation.

Table 11: The mean and maximum value of the average error for five observers in x direction, e_x, y direction, e_y, error magnitude, $\|\boldsymbol{e}\|$, standard deviation, Std and displacement, Disp, over the twenty markers for case 1 to case 6. All values are in pixels.

Case	e_x mean/max	e_y mean/max	$\|\boldsymbol{e}\|$ mean/max	**Std** mean/max	**Disp** mean/max
1	0.4/2.3	0.0/1.4	1.0/2.7	1.0/2.4	11.5/17.9
2	0.4/3.0	-0.3/3.0	1.3/4.2	1.0/3.2	10.1/21.4
3	-0.1/2.1	0.0/5.3	1.4/5.4	1.4/3.8	11.0/18.8
4	-0.1/1.1	0.0/0.9	0.6/1.1	0.5/0.9	8.1/11.1
5	-0.4/2.8	0.5/2.4	1.0/3.4	0.8/2.6	12.1/21.3
6	-0.2/1.0	0.1/1.3	0.7/1.7	0.7/1.3	7.6/15.2

Table 12: The mean and maximum error value of markers with salient anatomical features for cases 1 to 6. All values are in pixels.

Case	e_x mean/max	e_y mean/max	$\|\boldsymbol{e}\|$ mean/max	**Std** mean/max	**Disp** mean/max
1	0.4/2.0	-0.1/1.1	1.0/2.0	0.8/1.3	11.1/17.9
2	0.4/1.3	-0.2/1.1	0.9/1.4	0.9/3.2	12.2/21.4
3	0.2/1.2	0.3/1.2	0.9/1.7	0.8/1.7	11.3/17.2
4	-0.0/0.8	0.0/0.9	0.6/0.9	0.5/0.9	8.8/11.1
5	-0.5/1.3	0.2/1.0	0.7/1.4	0.6/1.3	9.6/17.5
6	-0.1/0.9	0.1/0.7	0.6/1.0	0.5/1.0	8.5/15.2

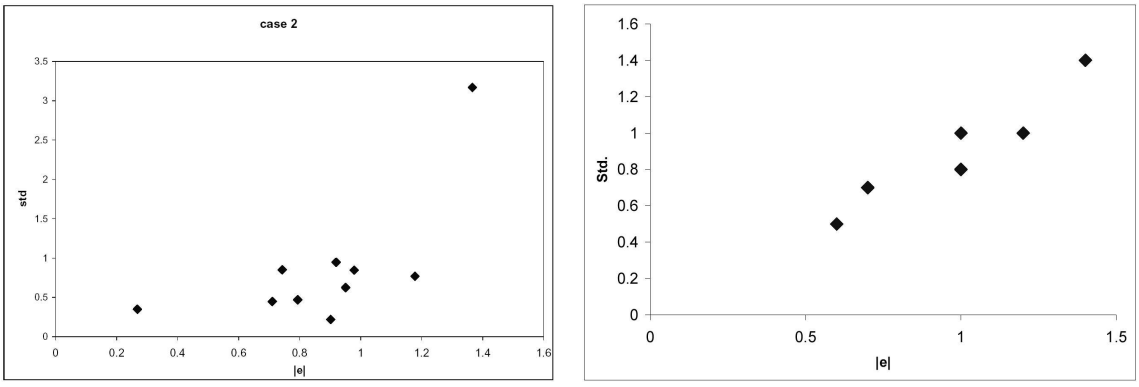

(*a*) (*b*)

Figure 26: (a) A sample scatter plot of the standard deviation versus error for case 2 of markers with salient anatomical features. (b) The scatter plot of the average value of the mean standard deviation versus the errors for all six cases.

Table 13: The correlation coefficient of standard deviation and error for markers with salient anatomical features from case 1 to case 6.

Case	**1**	**2**	**3**	**4**	**5**	**6**
Correlation coefficient	-0.09	0.67	0.77	0.39	0.73	0.56

Table 14: The mean and maximum value of the average error for four observers in x direction, e_x, y direction, e_y, z direction, e_z, error magnitude, $\|\boldsymbol{e}\|$, and standard deviation, Std over the twenty markers. All values are in millimeters.

Case	e_x	e_y	e_z	$\|\boldsymbol{e}\|$	**Std**
	mean/max	mean/max	mean/max	mean/max	mean/max
1	-0.1/6.7	0.0/2.1	0.3/2.6	1.5/6.7	1.4/10.8

6.4.2 3D validation strategy

For the 3D case, the result of the same statistical analysis as in the 2D cases is shown in Table 14 but only for 20 validation points for one case. The mean errors in x, y and z direction are between -0.1 and 0.3 mm, but the maximal error is 6.7 mm in x direction for one of the points. Due to the proximity of a dark small region to a bead, observers may have mistaken the dark region for the bead. The Std is highly correlated with the mean error magnitude, and the correlation coefficient between these two variables is .96.

CHAPTER 7

DISCUSSION AND CONCLUSION

Nonrigid medical image registration can serve as a powerful tool for combining information from multiple imaging modalities, monitoring changes in size, shape, or image intensity over time intervals, relating preoperative images and surgical plans to the physical reality of the patient in the operating room during image-guided surgery, and relating an individual's anatomy to a standardized atlas.

In this thesis we have defined the registration problem and given a general survey of the registration methods. An introduction to some common methods are given and the nonrigid registration methods have been further discussed. The intensity-based approach is preferable for automatic registration because it alleviates the need for a difficult feature detection step. The mean square differences and normalized mutual information are reasonable measures of the quality of the fit, and we have found it to perform well both in the 2D and 3D applications. Thin-plate spline and cubic B-spline have good warping properties and lend themselves well to a multi-scale optimization strategy. The described automatic algorithm takes advantage of all these properties; it is robust, efficient, and has been tested on different deformation patterns both in 2D and 3D simulations.

We also have proposed a method for achieving transitivity and symmetry of image registration algorithms. Transitivity and symmetry are desired properties that should be satisfied by any image registration algorithm. We have implemented the proposed method and quantitatively tested it on a sequence of images. The transitivity and symmetry error can be made arbitrary small, since they are directly affected by the error of numerical computation of the inverse transform. In our tests on triples of images from short axis cardiac MR image sequences, the maximal transitivity error of the 2D experiments was $9.0 \cdot 10^{-6}$ of a pixel and the 3D experiments was $2.2 \cdot 10^{-4}$ of a voxel. For the symmetry tests, the maximal transitivity error of the 2D experiments was $4.8 \cdot 10^{-6}$ of a pixel and the 3D

experiments was $6.5 \cdot 10^{-4}$ of a voxel. In this research, we have theoretically and practically demonstrated that the proposed method indeed achieves transitivity and symmetry of a nonrigid image registration algorithm. It remains to be tested if the proposed approach improves the registration accuracy over nonrigid image registration algorithms that are not transitive or symmetric. The drawback of the presented method, in addition to the computation of the inverse transform, is the requirement of registering through a "model", which limits the registration to be performed on a sequence of images and not available for registering only between two images.

The method for obtaining validation data for nonrigid image registration algorithms is similar to simulations in the sense that the deformation is artificial. However, the images are obtained using a real acquisition system, rather than applying a mathematical model. By changing the optical warper and the clay model we can generate various 2D and 3D deformation patterns respectively. While these phantom validation studies do not provide physically correct deformations, they are certainly a useful way to test the ability of registration algorithms to recover various deformation patterns.

The analysis of the manual validation showed that the observers, when averaged, were able to come close in accuracy to the presented methods (both in 2D and 3D) for points located at strong image features, while they produced much less accurate results for points in image regions with poor or no features. At the other hand, the presented methods generate equally accurate validation data everywhere in the image regardless of the strength of the image features. Another finding was that the standard deviation (over the observers) was not a reliable prediction of error for single points, while when averaged over all the points in the set it was highly correlated with the mean error of the points. These conclusions can be used as guidelines when designing validation strategies for nonrigid image registration algorithms based only on the input of observers.

REFERENCES

[1] Joseph V. Hajnal, Derek LG Hill, and David J. Hawkes, "Medical Image Registration" CRC Press, Boca 2001.

[2] Bookstein, F.L., 1989. Principal warps: Thin-plate splines and the decomposition of deformations. *IEEE Trans. Pan. Anal. Mach. Intell.* 11 (6), 567-585.

[3] Amit, Y., "Graphical shape templates for automatic anatomy detection with applications to MRI brain scans", *IEEE Trans. Med. Imaging* 16 (1), 28-40, 1997.

[4] Davis, M.N., Khotanzad, A., Flamig, D.P., Harms, S.E., 1997. "A physics based coordinate transformation for 3D image matching", *IEEE Trans. Med. Imaging* 16 (3), 317-328.

[5] Subsol, G., Thirion, J. P., and Ayache, N., "A general scheme for automatically building 3-D morphometric anatomical atlases: Application to a skull atlas", *Med. Image Anal.*, vol. 2, no. 1, pp. 37-60, 1998.

[6] Ge, Y., Fitzpatrick, J.M., Kessler, R.M., Jeske-Janicka, M., "Inter- subject brain image registration using both cortical and subcortical landmarks". In: Proceedings Image Processing, SPIE 2434, pp. 81-95, 1995.

[7] Can, A., Stewart, C.V., Roysam, B., Tanenbaum, H.L., "A Feature-Based, Robust, Hierarchical Algorithm for Registering Pairs of Images of the Curved Human Retina", *IEEE Trans. on Pattern Analysis and Machine Intelligence*, Vol. 24, No. 3, March 2002.

[8] Szeliski, R. and Lavallee, S., "Matching 3-D anatomical surfaces with nonrigid deformations using octree-splines", *SPIE Geometric Meth. Comput. Vis.*, vol. 2031, pp. 306-315, 1993.

[9] Thompson, P.M., Toga, A.W., "A surface-based technique for warping 3 dimensional images of the brain", *IEEE Trans. Med.* 15 (4), 402-417, 1996.

[10] Audette, M.A., Ferrie, F.P., Peters, T.M., " An algorithmic overview of surface registration techniques for medical imaging", *Medical image Analysis* 4 (2000) 201-217.

[11] Ashburmer J, Neelin P, Collins DL, Evans AC, Friston KJ, "Incorporating Prior Knowledge into Image Registration", *Neuroimage* 6(4):344-352, 1997.

[12] Woods RP, Grafton ST, Watson JDG, Sicotte NL, Mazziotta JC. "Automated image registration:II. Intersubject validation of linear and nonlinear models", *J of Computer Assisted Tomography*, 22:153-165, 1998.

[13] Collins, D.L., Holmes, C.J., Peters, T.M., and Evans, A.C., "Automatic 3D model-based neuroanatomical segmentation". Human Brain Mapping, 3:190-208, 1995.

[14] Kim, B., JL Boes, KA Frey and CR Meyer. "Mutual information for automated unwarping of rat brain autoradiographs". *NeuroImage* 5(1):31-40, 1997

[15] Christensen, G.E., Joshi, S.C., and Miller, M.I., "Transformation of Brain Anatomy", *IEEE Trans. on Medical Imaging* 16:6; 864-877, 1997.

[16] Yoshida, H., "Removal of normal anatomic structures in radiographs using wavelet-based non-linear variational method for image matching", *Wavelet Applicant. Signal Imaging Process.*, Vol 3458, pp. 174-181, 1998.

[17] Wu, Y., Kanade, T., Li, C., and Cohn, J., "Image registration using wavelet-based motion model", *International Journal of Computer Vision*, 38(2), 2000.

[18] Meyer, C.R., Boes, J.L., Kim, B., Bland, P.H., Zasadny, K.R., Kison, P.V., Koral, K., Frey, K.A., and Wahl, R.L., "Demonstration of accuracy and clinical versatility of mutual information for automatic multimodality image fusion using affine and thin-plate spline warped geometric deformations", *Med Image Anal.* 1997. Apr;1(3):195-206.

[19] Rohr, K., Stiehl, H.S., Buzug, T.M., Weese, J., Kuhn, M.H., "Landmark-based elastic registration using approximating thin-plate splines", *IEEE Trans. on Medical Imaging* 20; 526-534, 2001.

[20] Mattes, D., Haynor, D.R., Vesselle, H., Lewellen, T.K., and Eubank, W., "PET-CT image registration in the chest using free-form deformations", *IEEE Trans Med Imaging*, Jan; 22(1): 120-8, 2003.

[21] Rodhe, G., Aldroubi, A., and Dawant, B., "The Adaptive Bases Algorithm for Intensity Based Non Rigid Image Registration", *IEEE Trans. on Medical Imaging*, Vol. 22, No. 11, November 2003.

[22] Rohlfing, CR Maurer, Jr., DA Bluemke, and MA Jacobs, "Volume-Preserving Nonrigid Registration of MR Breast Images Using Free-Form Deformation With an Incompressibility Constraint", *IEEE Trans Med Imaging*, Jun; 22(6):730-41, 2003.

[23] Gee, J.C., Reivicj, M., and Bajcsy, R., " Elastically deforming 3-D atlas to match anatomical brain images", *J. Comput. Assist. Tomogr.*, vol. 17, no. 2, pp. 225-236 1993.

[24] Davatzikos, Ch., "Spatial transformation and registration of brian images using elastically deformable models", *Comput. Vis. Image Understanding*, vol. 66, no. 2, pp. 207-222, 1997.

[25] Christensen, G., Rabbitt, R., and Miller, M., "Deformable templates using large deformation kinematics", *IEEE Transactions on Image Processing*, 5(10):1435V1447, Oct 1996.

[26] Bro-Nielsen, M. and Gramkow, C., "Fast fluid registration of medical images", In KH. Hohne and R. Kikinis, editors, Proc. Visualization in Biomedical Computing, number 1131 in Lect. Not. in Comp. Sci., pages 267–276. Springer, September 1996.

[27] Thirion, J.P., "Image matching as a diffuse process: An analogy with Maxwell's demons", *Med. Image Anal.*, vol. 2, pp 243-260, 1998.

[28] Hellier, P., Barillot, C., Memin, E., and Perez, P., "Hierarchical Estimation of a Dense Deformation Field for 3-D Robust Registration", *IEEE Trans. on Medical Imaging*, 20(5), pp 338-402, 2001.

[29] Rueckert, D., Sonoda, L.I., Hayes, C., Hill, D.L.G., Leach, M.O., and Hawkes, D.J., "Nonrigid registration using free-form dformations: Application to breast MR images", *IEEE Transactions on Medical Imaging*. Vol. 18, No. 8, pp 712-721, August 1999.

[30] Wahba, W., "Spline models for observational data", Soc. Industr. Applied Math., 1990.

[31] Hajnal, J.B., Saeed, N., Oatridge, A., Young, I.R. and Bydder, G.M., "Detection of subtle brain changes using subcoxel registration and substraction of serial MR images", *J. Comput. Assist. Tomogr.*, 19 677-91, 1995.

[32] Hajnal, J.B., Saeed, N., Soar, E.J., Oatridge,A., Young, I.R. and Bydder, G. M., " A registration and interpolation procedure for subvoxel matching of serially acquired MR images", *J. Comput. Assist. Tomogr.*, 19 289-96, 1995.

[33] Lemieux, L. and Barker, G.J., "Measurement of small inter-scan fluctuations in voxel dimensions in magnetic resonance images using registration", *Med. Phys.*, 25 1049-54, 1998. Josien P.W.

[34] Pluim, J.B., Antoine Maintz, Max A. Viergever, "Mutual Information Based Registration of Medical Images: A Survey", *IEEE Transactions on Medical Imaging*, Volume 22, Number 8, August 2003.

[35] Christensen, Gary E., "Consistent Linear-Elastic Transformations for Image Matching", *IPMI*, 224-237, 1999.

[36] Christensen, G.E., Johnson, H.J., "Consistent Image Registration", *IEEE Transactions on Medical Imaging.*, 20(7), pp. 568-582, July 2001.

[37] Johnson, H.J., Christensen, G.E., "Consistent Landmark and Intensity-based Image Registration", *IEEE Transactions on Medical Imaging*, 21(5), pp. 450-461, 2002.

[38] Christensen, G.E., Johnson, H.J., "Invertibility and Transitivity Analysis for Nonrigid Image Registration", *Journal of Electronic Imaging*, Vol. 12(1), January 2003.

[39] Skrinjar, Oskar and Tagare, Hemant, "Symmetric, Transitive, Geometric Deformation and Intensity Variation Invariant Nonrigid Image Registration", *ISBI*, Arlington, VA, April 2004.

[40] Skrinjar, O., Chou, Y., and Tagare, H. "Transitive Nonrigid Image Registration: Application to Cardiac MR Image Sequences", *SPIE Medical Imaging*, February 2004, San Diego, CA.

[41] Fitzpatrick, J.M., Hill, D.L.G, Shyr, Y., et al., "Visual assessment of the accuracy of retrospective registration of MR and CT images of the brain", *IEEE Trans. Med. Imag*, 17: 571-585, 1998.

[42] Barber, D.C., Tindale, W.B., Hunt, E., et al.,"Automatic registration of SPECT images as an alternative to immobilization studies", *Physics in medicine and biology*, 40:449-463, 1995.

[43] Joshi, S.C. and Miller, M.I., "Landmark Matching via Large Deformation Diffeomorphisms", *IEEE Transactions on Image Processing*, 9(8), pp. 1357-1370, 2000.

[44] Rabbitt, R.D., Weiss, J., Christensen, G., et al., "Mapping of hyperelastic deformable templates using the finite element method", *Proc. of SPIE, International Symposium on Optical Science, Engineering, and Instrumentation*, vol. 2573, pp. 252-265, 1995.

[45] Thirion, J. -P., "Image matching as a diffusion process: an analogy with Maxwell's demons", *Medical Image Analysis*, Vol. 2, Issue: 3, pp. 243-260, 1998.

[46] Ferrand, M., Warfield, S., Nabavi, A., et al., "Registration of 3D intraoperative MR images of the brain using a finite element biomechanical model", *Medical Image Computing and Computer-Assisted Intervention MICCAI'2000*, Vol. 1935, pp. 19-28, 2000.

[47] Hagemann, A., Rohr, K., Stiehl, H.S., et al., "Biomechanical modeling of the human head for physically based, nonrigid image registration", *IEEE Trans. on Medical Imaging*, 18(10): 875-884, 1999.

[48] Maurer CR. Jr, Fitzpatrick JM., Wang MY., et al., "Registration of head volume images using implantable fiducial markers", *IEEE Trans. Med. Imag*, 16(4): 447-462, 1997.

[49] West, J., Fitzpatrick, J.M., Wang, M.Y., et al., "Comparison and evaluation of retrospective intermodality brain image registration techniques", *Journal of Computer Assisted Tomography*, 21(4): 554-566, 1997.

[50] Rohr, K., Fornefett, M., and Stiehl, H.S., "Approximating thin-plate splines for elastic registration: integration of landmark errors and orientation attributes", In A. Kuba, M. Samal, and A. Todd-Pokropek, editors, *Information Processing in Medical Imaging: Proc. 16th International Conference (IPMI'99)*, volume 1613 of Lecture Notes in Computer Science, pages 252-265. Springer Verlag, 1999.

[51] Schnabel, Julia A., Christine Tanner, Andy D. Castellano Smith, et al., "Validation of Non-rigid Registration Using Finite Element Methods: Application to Breast MR Images",*IEEE Trans. Med. Imag*, 22(2): 238-247, 2003.

[52] Freeborough, P.A., Woods, R.P. and Fox, N.C., "Accurate registration of serial 3D MR brain images and its application to visualizing change in neurodegenerative disorders", *J. Comput. Assist. Tomogr*, 20: 1012-1022, 1996.

[53] Holden, M., Hill, D.L.G., Denton, E.R.E., et al., "Voxel similarity measures for 3D serial MR image registration", *IEEE Trans. Med. Imag*, 19: 94-102, 2000.

[54] Axel, L., "Physics and technology of cardiovascular MR imaging", *Cardiology Clinics*, 16(2):125-133, 1998.

[55] Pelc, N., et al., "Phase contrast cine magnetic resonance imaging", *Magnetic Resonance Quarterly*, 7(4):229-254, 1991.